Passive Radar Array with Low-Power Satellite Illuminators Based on Fractional Fourier Transform

Zhongyu Li, Fabrizio Santi, Debora Pastina, Pierfrancesco Lombardo

Abstract—**This paper addresses the detection of surface slow moving targets by means of an array passive radar based on low-EIRP satellite illuminators of opportunity. Particularly, the use of the receiving array of K elements is considered to provide increased detection capability for targets with limited radar cross section, together with the capability to estimate the target direction-of-arrival (DOA). A full processing scheme is proposed to exploit together both the long integration times and the multiple receiving elements. This includes a coherent space-time integration of the signal received at the K antenna elements during short frames, followed by an incoherent frame to frame integration.**

The proposed scheme is based on the Fractional Fourier Transform (FrFT) that is shown to map the signals into a natural rotated frequency-angle plane, where we can easily compensate the target Doppler frequency shifts available at the different antenna elements and temporal frames. Its effectiveness is shown by application to different synthetic scenarios, where the target detection is only achievable when all the possible integration gain is capitalized.

Index Terms—**passive bistatic radar, moving target detection, DOA estimation, Fractional Fourier Transform, satellite-based passive radar**

I. INTRODUCTION

THE last two decades have seen a significant growth of interest in passive radar sensors for surveillance applications. Passive radar sensors do not emit any e.m. radiation; they capitalize on the signals already existing in the environment, often referred to as signals of opportunity. The absence of the transmitting section makes them lighter than conventional radar systems and totally "green" since they do not contribute to the e.m. environmental pollution, hence they can be deployed in places where heavy active radar cannot be installed or undesired for their harmful radiations. Moreover, the absence of transmission provides intrinsic covert operation, as well anti-jamming and anti-stealth capabilities, [1].

The large majority of the developed passive radar technologies considers terrestrial transmitters as signal sources. The large number of RF emissions from terrestrial illuminators results in a wide range of signal types, which in many cases, e.g. the FM radio, can have relatively high transmitter power

[2], as well as the possibility to exploit different channels emitted by the same broadcast station [3]. The exploitation of television broadcast towers has become quite effective since a significant fraction of the world has switched to digital transmissions, with applications both to air and maritime traffic surveillance, [4], [5]. Also mobile phone base stations, as well as Wi-Fi, WiMAX/LTE, and all OFDM modulated transmissions have been investigated toward new fields of application, varying from the surveillance of local areas up to the monitoring of people in indoor environment [6]-[11].

Critical factors affecting terrestrial-based passive radar are multipath and shadowing effects, as well as the reliance on potentially vulnerable proximate infrastructure. A very promising option is relying on satellite illuminators, [12], [13]. Unlike terrestrial sources, satellite signals are not blocked by mountains and are less sensitive to multipath issues. Some theoretical and experimental studies have been conducted in the past exploiting communication and navigation satellites [12]-[14], with particular regard to the imaging of stationary scenes [15]-[20]. Wide accessibility on the global scale as well as the launching of new satellite fleets (such as the European navigation satellite system Galileo) are stimulating the research toward new generation of passive radar sensors [21]-[23].

Maybe one of the frameworks that more enjoys the exploitation of satellite sources is the maritime surveillance. Satellite-based illuminators such as DVB-S, Inmarsat and GNSS constellations have the potential to provide a persistent monitoring even of economic ocean zones and adjacent waters. Continental coverage is assured by geosynchronous satellites transmitting in DVB-S, while GNSS signals are available everywhere over the Earth's surface: even at the poles. Therefore, a ship navigating near the coastline or in open sea can be reached by the radio waves emitted by non-cooperative satellite illuminators and the reflections can be intercepted by light receivers carried by platforms mounted on the coast or on moored buoys.

In order to sort the reflected signals into the capability to detect a target, sophisticated signal processing techniques have to be developed, able to deal with the specific issues of the considered scenario and application. One of the biggest challenges when satellite sources are employed as illuminators of opportunity is the very low level of electromagnetic field on

the Earth's surface, thus requiring very long integration times to improve the signal level by means of integration. Passive radar relying on terrestrial transmitters usually use long coherent processing intervals (CPI) in the order of hundreds of milliseconds to detect aerial and naval targets. However, the exploitation of satellite signals of opportunity makes necessary to enlarge the dwell time on target up to several tens of seconds to strengthen the reflected signal energy sufficiently for the target detection. As example, in [14] integration times longer than 30 s are shown to be needed to achieve a signal-to-noise ratio (SNR) of about 12 dB for a target with radar cross section of 10 dB 40 km away from the receiver, referring to a geostationary satellite of the Eutelsat fleet. When lower EIRP (Equivalent Isotropic Radiated Power) sources, such as GNSS [24], are considered, the moving target detection task can be even more challenging; while big targets can be detected by exploiting integration times in the order of few seconds, as in [25] and [26] referred to the Galileo fleet, in [27] and [28] integration times of approximately 1 min are shown to be needed for the detection of a very small ship target (about 10 m length) less than 1 km away from the receiver exploiting GNSS transmitters of the GLONASS fleet.

The classical approach for moving target detection is the Doppler filtering, which in most of passive radar systems consists in detecting a peak in the relative time delay-Doppler plane obtained over short dwell times. However, when the integration time increases sensibly to detect targets with lower radar cross section, the Doppler frequency is no longer constant during the processing interval and exhibits time-varying characteristics. This makes the classical Doppler filtering techniques unsuitable, since the signals move through the Doppler filters. Multiple tools that have been developed in the past to deal with signals of this type belong to the category of the time-frequency distributions, such as the Wigner-Ville Distribution [29]. To develop an appropriate technique to deal with such long integration times we resort to a generalization of the Fourier Transform (FT), known as Fractional Fourier Transform (FrFT) [30]. While the FT decomposes the signals in terms of a set of orthogonal sinusoids, the FrFT decomposes the signals in terms of a basis formed by chirped waveforms; thus it can highly concentrate the energy distribution of linear frequency modulated (LFM) signals into a single point. Over the last years, the radar community investigated its utilization for different purposes, such as moving target detection, imaging and waveform generation, [31]-[35].

In the specific context of moving target detection based on long integration times, the Doppler frequency variation with time can be generally approximated with a linear term, by arresting the standard Taylor expansion series to the first order. Therefore, a frequency modulated LFM signal is obtained, namely a chirped waveform, and the FrFT is especially appropriate to concentrate its energy distribution into a single position. In previous research [36], it has been shown how the FrFT can be successfully employed in satellite-based passive radar sensors for the detection of moving targets with long integration times. Working in conjunction with the Keystone reformatting, the method in [36] exploits the kernel of the fractional transform to drive a hybrid coherent/non-coherent integration of the signal energy available inside a long stream of data. Such a technique is able to detect targets that cannot be identified with conventional (i.e., short integration time) detection techniques in the space-based system under consideration. However, despite the increased performance obtained by exploiting the long integration time, only targets with sufficiently high radar cross section can be detected. Moreover, only a very limited localization accuracy of the detected targets is available. Indeed, the technique allows only retrieving the bistatic ranges; thus, it enables positioning them on the locus of points given by the intersection of the bistatic ellipses with the area illuminated by the receiving antenna.

In the present paper, we investigate the possibility to improve the achievable performance by exploiting an array of receiving antennas that collect multiple target-scattered signals. The array configuration presents several interesting advantages, such as (i) the higher SNR level achievable by exploiting coherently the multiple receiving channels; (ii) the capability to measure the target direction-of-arrival (DOA), thus increasing the localization accuracy of the system. While the extension from a single to multiple receiving elements is conceptually simple, the overall processing technique that is required to exploit the array benefits is not trivial. Specifically, the proposed processing technique requires essentially a search in a 3D parameter space, in lieu of the 2D search presented in [36], the target DOA being the additional search parameter. Therefore, the highest integration gain is obtained for the actual target DOA, which also provides the DOA estimate.

Among the key points of the new processing technique, we need to mention that the FrFT domain still appears as a natural domain to perform the target coherent integration, whereas it is apparent that the signals received at different antenna elements provide a peak in the FrFT plane in a different position. In consequence, the spatial integration of the echoes received at different antenna elements requires not only a phase compensation, but also an appropriate re-alignment of the FrFT maps. In turn, this requires to be effectively implemented, so that the different possible approaches to apply the re-alignment are considered.

The remainder of the paper is organized as follows. The signal model for the receiving array is introduced in Section II, together with a brief description of the single–receiver processing scheme. This also includes a brief recall of the FrFT. The proposed target detection and DOA estimation technique is presented in Section III, where the required shift and phase compensations are identified. The effectiveness of the developed technique is widely tested and demonstrated in Section IV for different study cases. Finally, in Section V we draw our conclusions.

II. Signal Model and Single Receiver Processing

A sketch of the reference scenario for the satellite-based passive radar considered in this paper is reported in Fig. 1 with reference to a maritime surveillance application. In this case, T_X is the satellite opportunistic transmitter, R_X is the ground based stationary receiving array and the target is a vessel with speed
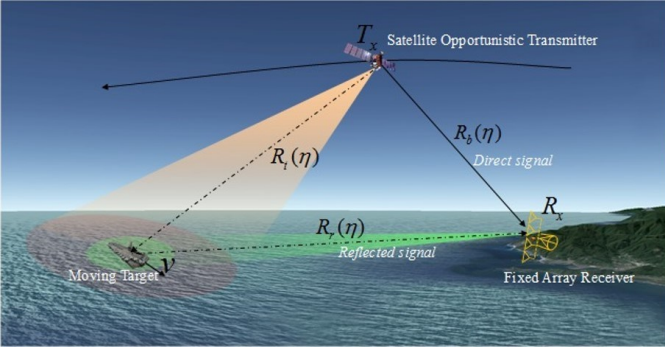
Fig. 1. Reference surveillance scenario.

V and direction θ (measured with respect to the R_X line-of-sight, LOS). Three distances are involved in this case: (i) the baseline, R_b, i.e. the distance between the transmitter and the center of the receiving array, (ii) the distance R_t between T_X and target, and (iii) the distance R_r between the target and the receiving array. It is assumed that both transmitter and target are in motion, so that all three distances change with time.

The passive radar consists of a receiving only device consisting of a linear array of K equi-spaced receiving surveillance antennas acquiring the reflected signal from the area where targets are looked for, plus a reference antenna steered toward the T_X to acquire a copy of the transmitted signal. This is used as the reference signal for the matched filter.

The top-view and the three-dimensional view of the system geometry are sketched in Fig. 2. We assume that the array receiver is centred in the origin of the (O, x, y, z) reference system, where also the reference antenna is located. A satellite is assumed flying over the surveyed area with instantaneous coordinates $[x_T, y_T, z_T]$, which identify the satellite aspect angle θ_T (measured with respect to the R_X LOS) and elevation angle ψ_T, both possibly changing with time. The array line-of-sight is along the x axis (identified by the unit vector $\hat{x}$), whereas the array elements are aligned along the y axis (direction of the unit vector $\hat{y}$), so that the position of the kth receiving element, with k = -K/2,…,K/2-1 and an even value of K for simplicity, is given by $(0, y_k, 0)$ where $y_k = [kd + d/2]$, being d the inter-element distance. As apparent, the array inter-element distance d must be set imposing that grating lobes will occur outside the antenna beamwidth Θ [37].

We assume a target, such as a ship, within the antenna footprint for the entire dwell time T_a. We further assume that the array and the target are coplanar. Therefore, the target instantaneous position can be expressed as $p(\eta) = p_0 + v \cdot \eta = [x_0, y_0] + [v_x, v_y] \cdot \eta$, where $\eta \in \left[-\frac{T_a}{2}, \frac{T_a}{2}\right]$ is the slow-time. $\theta_0 = \tan^{-1}\left\{\frac{p_0 \cdot \hat{y}}{p_0 \cdot \hat{x}}\right\}$ denotes the target DOA at the reference time, which will be objective of the estimation technique proposed in this paper.

After range compression, the data received by the kth element of the array in the range&slow-time (r, η) domain can be modelled as follows

$$s_k(r, \eta) = \sigma_\eta rect\left[\frac{\eta}{T_a}\right] \cdot \exp\left\{-j\frac{2\pi}{\lambda}R_k(\eta)\right\} \cdot \rho[r - R_k(\eta)] \quad (1)$$
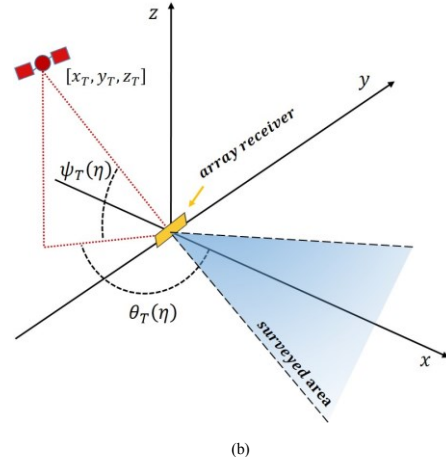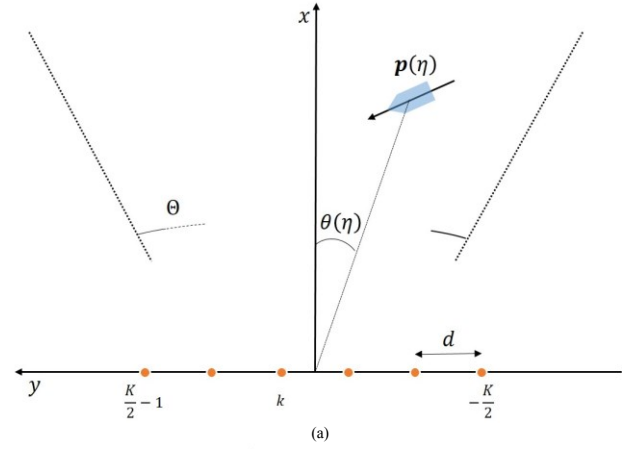

(a)

(b)

Fig. 2. Top-view (a) and three-dimensional view (b) of the system geometry.

In the above equation, $\rho(\cdot)$ is the cross-correlation function between reflected and reference signal, which specific shape depends on the particular satellite transmitter. λ is the carrier wavelength and σ_η is the complex reflectivity of the target possibly changing with slow-time. $R_k(\eta)$ is the differential bistatic range measured by the kth element that can be expressed as

$$R_k(\eta) = R_{Tx}(\eta) + R_{Rx^k}(\eta) - R_b(\eta) \quad (2)$$

where R_{Tx} and R_{Rx^k} are the transmitter to target and target to kth element distances, respectively, and R_b is the transmitter to array baseline; because of the target motion, as well as possible transmitter motion, such distances change with time. By expanding (2) into second order Taylor series, we get

$$R_k(\eta) \cong R_k^0 - \lambda \bar{f}_k^{dc}\eta - \lambda \bar{f}_k^{dr}\frac{\eta^2}{2} \quad (3)$$

where R_k^0 is the bistatic range at the reference instant and $\bar{f}_k^{dc}$ and $\bar{f}_k^{dr}$ are the Doppler Centroid (DC) and the Doppler Frequency Rate (DFR) of the target. Due to the large distance between transmitter and both target and receiver array, we can assume that all the elements of the array measure the same DFR, i.e. $\bar{f}_k^{dr} \cong \bar{f}_0^{dr} = \bar{f}^{dr}$. Therefore, the received signal expression in (1) can be rewritten as

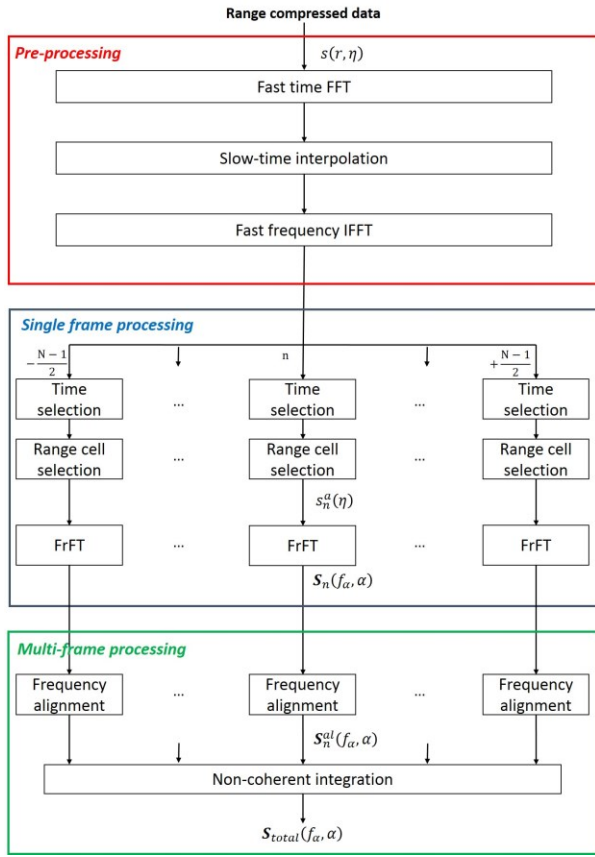$$s_k(r, \eta) = \sigma_\eta rect\left[\frac{\eta}{T_a}\right] \cdot$$

Fig. 3. Single-receiver integration block diagram.

$$\exp\left\{-j\frac{2\pi}{\lambda}\left(R_k^0 - \lambda\bar{f}_k^{dc}\eta - \lambda\bar{f}^{dr}\frac{\eta^2}{2}\right)\right\}\cdot \quad (4)$$
$$\rho\left[r - \left(R_k^0 - \lambda\bar{f}_k^{dc}\eta - \lambda\bar{f}^{dr}\frac{\eta^2}{2}\right)\right]$$

Due to the limited EIRP emitted by the satellites, which only rely on solar panels as a source of energy, and to the long distance between transmitter and target, the level of the signal power scattered by the target and collected by the passive radar receiving elements is extremely low. Therefore, in order to detect the target, it is required to integrate the signals collected over a long integration time and at all receiving elements. From the signal model in (4) it is clear that both range and Doppler positions of the target vary during the dwell time and their values are different for different receiving antenna elements. Therefore, proper strategies need to be identified to compensate both range and Doppler frequency migrations before being able to perform the integration of the target echoes over the long integration time and different antenna elements. In addition, the integration strategy must take into account the target scattering behaviour that typically shows a temporal coherency limited to time intervals much shorter than the desired integration times.

The case of a single receiving antenna element was already analysed by the authors in [36], where a complete processing scheme has been devised and shown to be effective for the target echo signal integration. The block diagram of the integration technique is reported in Fig. 3. First, range compression is applied to the signal received at the surveillance channel. In general, this is implemented by subdividing the continuous received signal into small batches of T seconds each, and cross-correlating each batch with the corresponding batch of the signal received at the reference channel. T is selected to be small enough that phase rotation inside the batch is negligible (typical values for T are of the order of 10^{-3} s). This provides a sequence of range-compressed signal batches with temporal separation T, which is equivalent to the range-compressed data provided by a pulsed radar system operating with an equivalent PRF=1/T. In the specific case of exploitation of GNSS, the reference used for range compression should be a noise free replica of the reference signal regenerated according to the parameters of the direct signal (i.e. time-delay, Doppler frequency, phase and, if included, navigation message) retrieved by means of a proper synchronization technique, as described in [26]. Such procedure assures the direct compensation of any relative motion between the transmitting satellite and the receiver.

The processing scheme in Fig. 3 operates on these range-compressed data. It starts with a pre-processing stage aiming at removing the range cell migration (RCM) over the entire dwell time. Afterwards, the same processing algorithm can applied to each range resolution cell either sequentially or in parallel. The RCM corrected data are segmented into temporal frames short enough that the target echo can be considered coherent inside each one of them, namely it shows no phase and amplitude fluctuations. To perform a coherent integration inside each temporal frame (T_{CPI}), the Fractional Fourier Transform is applied to the individual range resolution cell, which maps the signal portion into the rotated frequency-angle plane. This is expected to provide a peak in the rotated frequency-angle plane location corresponding to the target Doppler frequency and slope; however, due to the low signal power level, this peak is typically not high enough to exceed the noise level in the map. To increase the peak level, an incoherent integration of the rotated frequency-angle maps obtained at the individual temporal frames is performed. However, since the target motion between temporal frames causes a shift of the target peak in this plane, a frequency alignment is required before the incoherent integration.

As apparent, two specific transformations are involved in the processing scheme presented in [36]. The Keystone Transform (KT) is used in the pre-processing stage to reformat the data, thus removing the linear coupling between range and frequency domain [38], i.e. it removes the range walk. The Fractional Fourier Transform is used inside the single frame processing stage to perform the coherent integration of the signal inside the individual temporal frame. While the KT is now a well-established tool to deal with the range walk and it has no direct impact on the integration of the echoes received at the multiple receiving elements, the FrFT has a key role for the array signal integration technique that we propose inside this manuscript. Therefore, it is useful to give first a brief overview of this transform for moving target detection purposes.

The echo azimuthal signals in (4) are chirp signals whose parameters (DC and DFR) depend on the target motion and, in the case of the present paper, also on the antenna index. As the chirp signal are characterized by a Doppler frequency that
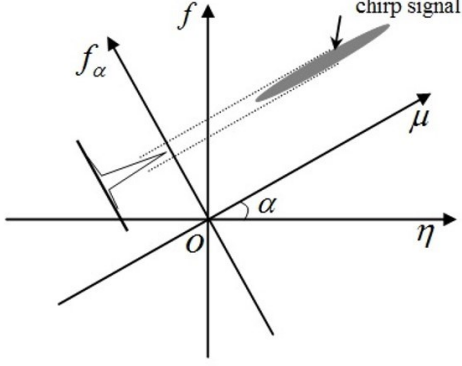
Fig. 4. Projection of a chirp signal onto the FrFT domain.

changes linearly with time, conventional coherent integration techniques relying on the Doppler filter banks (i.e., the FFT) cannot work properly, since the chirp signals thus migrate through resolution filters as a function of time. To perform a coherent integration of the chirp signals, it is necessary to estimate their chirp rate (DFR) and to consider this for the phase compensation. While many time-frequency distributions have been considered in the past, which can be exploited to estimate the chirp rate, the FrFT has the nice property to be a linear transformation. For this reason, it can be regarded as a generalization of the ordinary Fourier transform that includes a rotation over some arbitrary angle α in the time-frequency plane.

For ease of future reference, we recall that the FrFT of the generic signal $s(\eta)$ is obtained as, [30]:

$$s_\alpha(u) = \int_{-\infty}^{+\infty} s(\eta) \cdot B_\alpha(\eta, u) d\eta \qquad (5)$$

where u is the axis making an angle α with the time axis and $B_\alpha(\eta, u)$ is the transformation kernel defined as (6) shown bottom of this page.

Then, by Fourier transforming with respect to u, the signal is represented in the rotated frequency and rotation angle (f_α, α) domain:

$$S(f_\alpha, \alpha) = \int_{-\infty}^{+\infty} s_\alpha(u) \cdot e^{-j2\pi f_\alpha u} du \qquad (7)$$

The well-known projection of a chirp signal onto the fractional Fourier domain, [31], is depicted in Fig. 4. The result of this transformation applied to a chirp signal with DC equal to $\bar{f}^{dc}$ and DFR equal to $\bar{f}^{dr}$ is to concentrate the chirp energy in a specific point $(\bar{f}_\alpha, \bar{\alpha})$ of the FrFT plane, being $\bar{\alpha}$ the optimum rotation angle and $\bar{f}_\alpha$ the projected frequency centroid, which are characterized by the relationships:

$$\begin{cases} \bar{f}^{dc} = \dfrac{\bar{f}_\alpha}{\cos \bar{\alpha}} \\ \bar{f}^{dr} = \tan \bar{\alpha} \cdot \dfrac{PRF}{T_{CPI}} \end{cases} \qquad (8)$$

where PRF is the equivalent pulse repetition frequency of the system and T_{CPI} is the coherent processing interval over which the FrFT is computed.

We notice explicitly that if the signal energy received from the target during a single T_{CPI} were high enough with respect to the disturbance contributions, the peak of the FrFT would be clearly visible, which would make easy the estimation of the target motion parameters from the peak location, by means of (8). Under this assumption, the moving target could be detected by revealing the corresponding peak in the (f_α, α) domain. However, the restricted power budget provided by the satellites does not provide enough energy during T_{CPI}. Typically, this applies even when extending T_{CPI} up to the maximum target coherency time. Therefore, it is necessary to apply incoherent integration of multiple temporal frames to increase the global integration time, which could be in the order of several tens of seconds.

Due to the chirped characteristic of the overall received signal, from temporal frame to temporal frame the DC is changing with rate equal to DFR. This means that the peak location in the FrFT plane is moving as the temporal frame changes. However, its location can be easily predicted in this plane, since a peak at (f_α, α) at the first temporal frame moves to $(f_\alpha + n \sin \alpha \, PRF, \alpha)$ after n temporal frames; moreover, the displacement only depends on the initial FrFT coordinates and on the temporal frame index, n. Therefore, the incoherent integration can be performed effectively in the FrFT plane, after a compensation that does not require knowledge of additional parameters.

The above-summarized processing technique for the single surveillance receiver, which is strongly based on this property of the FrFT, is the basis for the derivation of the processing technique for the passive receiver array that is presented in the next section.

III. ARRAY RECEIVER FRFT-BASED TECHNIQUE

As anticipated in the introduction, this paper introduces a full processing scheme for an array passive radar with K surveillance receiving elements (that are complemented with the standard reference receiving channel with the antenna steered toward the transmitter). The use of an array of K receivers, in lieu of the single surveillance receiving channel, provides two types of improvement with respect to the single surveillance channel case:

(i) The coherent integration of the target signal returns received at the K antenna elements is expected to provide an increase of the final SNR by a factor K. Despite this improvement is far from unexpected, in our case of interest of a low-power satellite transmitter used as source of opportunity it might be essential to allow detection of the specific targets of interest. For example, using an array of K=10 receivers allows

$$B_\alpha(\eta, u) = \begin{cases} \delta(\eta - u) & \text{if } \alpha \text{ is a multiple of } 2\pi \\ \delta(\eta + u) & \text{if } (\alpha + \pi) \text{ is a multiple of } 2\pi \\ \sqrt{\dfrac{1 - j \cot \alpha}{2\pi}} \cdot e^{j \frac{u^2 + \eta^2}{2} \cot \alpha} \cdot e^{-ju\eta \csc \alpha} & \text{if } \alpha \text{ is not a multiple of } \pi \end{cases} \qquad (6)$$

the detection of vessels with bistatic cross-section 10 dB lower than in the case of the single receiver.

(ii) The receiving antenna array provides a DOA estimation capability, which is not available with the single receiver. This is quite essential to provide a target localization that does not reduce simply to the locus of points on a bistatic ellipse limited by the receiving antenna aperture. Specifically, using K antenna receivers, in principle a target resolution in the angle of arrival can be obtained up to 1/K of the receiving antenna beam, thus allowing separating multiple targets potentially present on the same bistatic ellipse. Moreover, a proper estimation can be provided for the target DOA with respect to the receivers, with an accuracy depending on the SNR.

We explicitly notice that, due to the long integration times required by the satellite-based passive radar, the target DOA cannot be estimated by using a rotating antenna beam (as in sensors based on relatively short integration times). In fact, a staring antenna is essentially required to provide such long observation frames.

As apparent from the model in Section II, moving from a single receiver to a receiver array of K elements is not trivial for this specific application. In fact, the Taylor expansion of the bistatic range in eq. (3) shows that together with the term of order zero, also the term of the first order depends on the antenna element k. Therefore, both phase and Doppler frequency depend on the considered antenna element k [see eq. (4)]. This implies that the coherent integration of the target signals received at the different antennas is not just obtained by a standard addition by a constant phase shift.

A different way to look at the problem is to consider that during the considered long integration times, the target DOA with respect to the receivers centre undergoes quite a clear change. This time-varying DOA must be appropriately compensated while the central DOA is estimated and the desired integration is obtained. This requires the derivation of the ad-hoc processing technique presented in this paper.

The proposed technique aims at integrating the signals received in order to synthetize the array over a long integration time, thus jointly enabling the target detection and the estimation of its DOA. In particular, a hybrid coherent/non-coherent procedure is performed. The former aims at synthetize the array over consecutive short time intervals (frames), whereas the latter performs an integration over the entire dwell time to strengthen the target energy thus counteracting the restricted power budget provided by the system under consideration. Therefore, two levels of integration can be identified: intra-frame, referring to the space-time coherent combination of the data of the array at the single frame levels, and frame-to-frame, referring to the combination of the data over the multiple frames. In the remainder of the section, it will be shown how both these integrations are performed in the DC-DFR domain, or better in the (f_α, α) domain, i.e. the domain obtained by means of the FrFT. In particular, it will be shown how the data combination in both the intra-frame and frame-to-frame domains can be driven by the kernel of this transform.

The processing can be organized in three macro-steps: pre-processing, intra-frame space-time coherent processing and multi-frame non-coherent processing. The detailed description is given as follows:

A. Pre-processing

The pre-processing aims at i) removing the RCM over the entire dwell time and ii) segmenting the RCM corrected data in short time frames for the array processing.

To deal with the RCM, we observe that in (3) $R_k^0 - R_0^0 \ll Kd \ll c/B$, being B the frequency bandwidth of the received satellite signal and c the speed of light. Therefore, we can assume $R_k^0 \cong R_0^0 = R^0$ inside the argument of ρ in (4). Moreover, by recalling that typically a reasonably small frequency bandwidth B is available, we assume that the second order terms inside the argument of ρ in (4) (i.e., the range curvature) are negligible. In consequence, our signal model can be approximated by:

$$s_k(r,\eta) = \sigma_\eta rect\left[\frac{\eta}{T_a}\right] \cdot$$
$$\exp\left\{-j\frac{2\pi}{\lambda}\left(R_k^0 - \lambda \bar{f}_k^{dc}\eta - \lambda \bar{f}^{dr}\frac{\eta^2}{2}\right)\right\} \cdot \quad (9)$$
$$\rho\left[r - \left(R^0 - \lambda \bar{f}_k^{dc}\eta\right)\right]$$

Using the above approximation, it is apparent that the range migration reduces to the linear term. The migration slope clearly depends on the antenna element k, so that the different receiving antennas are subject to a different type of migration. Keystone reformatting is the natural solution, which removes the linear coupling between range and frequency domain [38], i.e. it removes the range walk. Using KT, the range walk is removed independent of its slope, so that the application of this transform solves the problem for all receiving antenna elements. Therefore, as for the single channel case, [36], the use of the KT provides an effective pre-processing tool.

Even though additional processing could be exploited to remove the range curvature, as mentioned such a residual migration is expected to be smaller than one range resolution cell and therefore it can be ignored. In practice, this is obtained by applying a FT along the fast-time (range) domain to operate in the (f_τ, η) domain; interpolating to the new slow time variable $\breve{\eta}$ such that $\eta = \frac{f_c}{f_c + f_\tau}\breve{\eta}$ (being f_c the carrier frequency) and applying an inverse FT to come back in the $(r, \breve{\eta})$ domain, where the RCM corrected data can be expressed as:

$$s_k(r,\breve{\eta}) = \sigma_\eta rect\left[\frac{\breve{\eta}}{T_a}\right] \cdot$$
$$\exp\left\{-j\frac{2\pi}{\lambda}\left(R_k^0 - \lambda \bar{f}_k^{dc}\breve{\eta} - \lambda \bar{f}^{dr}\frac{\breve{\eta}^2}{2}\right)\right\} \cdot \rho[r - R^0] \quad (10)$$

We can observe that the signals in (10) are K slow-time phase modulated waveforms that have most of the energy gathered in a single range cell for the entire dwell time. We assume that the range cell containing the target echo has been selected and hereinafter the description is restricted to the azimuth signal only. Obviously, the same processing will be applied to each one of the range cells composing the surveyed area where a target is searched. Moreover, to simplify the notation from this point the modified slow time variable $\breve{\eta}$ will be written simply as η.

As mentioned in Section II, the RCS fluctuation prevents the

full coherent processing of the long dwell considered. Therefore, the data pertaining each element are segmented in N consecutive frames of limited duration such that within each frame constant reflectivity of the target can be assumed. Let $T_{CPI} = \frac{T_a}{N}$ be the duration of the individual frames, the signal pertaining to the kth antenna and the nth frame $\left(n = -\frac{N-1}{2}, ... \frac{N-1}{2}\right)$ is given by

$$s_{k,n}^a(\eta) = \sigma_n rect\left[\frac{\eta - n \cdot T_{CPI}}{T_{CPI}}\right] \cdot \exp\left\{-j\frac{2\pi}{\lambda}R_k(\eta)\right\} \quad (11)$$

Choosing a short T_{CPI}, the variation of the target reflectivity in (11) is supposed to be limited and thus it can be neglected; moreover, by defining a temporal variable $\eta' = \eta - n \cdot T_{CPI}$ that spans the single frame, we can rewrite:

$$s_{k,n}^a(\eta') = \sigma_n rect\left[\frac{\eta'}{T_{CPI}}\right] \cdot \exp\left\{-j\frac{2\pi}{\lambda}R_k(\eta' + n \cdot T_{CPI})\right\} \quad (12)$$

B. Intra-frame space-time coherent processing

Assuming that the target shows a constant cross section inside each temporal frame, the maximum SNR is provided by the coherent integration over the whole temporal frame spanned by η', namely of all the temporal samples $N_f = T_{CPI} \cdot PRF$, received at the K receiving antennas, namely a coherent space-time processing is required. However, to maximize the result of the coherent integration, the target differential bistatic range must be known as a function of time η' and antenna element k, so that the phase evolution with time can be compensated. This depends in turn on the target initial position (x_0,y_0) and on the target velocity (v_x,v_y). Since these parameters are unknown, it is necessary to estimate them from the received data. This can be obtained by attempting a coherent integration based on a grid of parameter values, and by selecting the combination of values that provides the maximum coherent integration. We first notice

that the target initial position (x_0,y_0) can be expressed in polar coordinates as target range and angle (r_0,θ_0). Since the processing is applied to every range cell, the r_0 value can be considered known and the maximization must be performed with respect to the three parameters (θ_0, v_x, v_y).

In [36], the use of the FrFT has been shown to be an effective tool to perform the coherent integration, inside each frame, of signals with generic DC and DFR. By means of the FrFT in (5)-(7), rotated frequency-angle maps are obtained, where the energy is maximally concentrated in the cell corresponding to the measured Doppler frequency and Doppler rate. Therefore, it is interesting to understand what is the effect of the FrFT applied to each of the N frames of the kth antenna. With this objective in mind, we expand the bistatic range for the kth antenna element into a Taylor series. The bistatic range in (2) can be rearranged as $R_k(\eta) = R_{Rx^k}(\eta) + \Delta R_{Tx-b}(\eta)$, being $\Delta R_{Tx-b}(\eta)$ the differential range history between R_t and R_b.

Let us consider first the target to kth element range. The series is arrested to the first order in the array element k, due to the small size of the receiving array: (13) shown bottom of this page.

Further, (13) is expanded in series as a function of the temporal variable. In this case, the series is arrested to the second order, since the range variation during the considered observation time can be relevant. Thus, we have (14) as shown bottom of this page.

For convenience, we define the radial and parallel velocity components respectively as: $v_r = v_x \cos\theta_0 + v_y \sin\theta_0$ and $v_p = v_x \sin\theta_0 - v_y \cos\theta_0$ and rewrite the range in (14), except for r_0, as a function of the three variables v_r, v_p, and θ_0, as (15) shown bottom of this page.

The differential range $\Delta R_{Tx-b}(\eta)$ takes into account the transmitter contribution to the range and Doppler history of the moving target. Observing that in the considered satellite-based

$$R_{Rx^k}(\eta) = \sqrt{x^2 + \left(y - \left(kd + \frac{d}{2}\right)\right)^2} = \sqrt{(r_0 \cos\theta_0 + v_x \eta)^2 + \left(r_0 \sin\theta_0 + v_y \eta - kd - \frac{d}{2}\right)^2} =$$

$$\cong \sqrt{(r_0 \cos\theta_0 + v_x \eta)^2 + (r_0 \sin\theta_0 + v_y \eta)^2} - \left(kd + \frac{d}{2}\right)\frac{(r_0 \sin\theta_0 + v_y \eta)}{\sqrt{(r_0 \cos\theta_0 + v_x \eta)^2 + (r_0 \sin\theta_0 + v_y \eta)^2}} \quad (13)$$

$$R_{Rx^k}(\eta) \cong r_0 + (v_x \cos\theta_0 + v_y \sin\theta_0)\eta + (v_x \sin\theta_0 - v_y \cos\theta_0)^2 \frac{\eta^2}{2r_0} - \left(kd + \frac{d}{2}\right)\sin\theta_0 +$$

$$+ \left(kd + \frac{d}{2}\right)\frac{\cos\theta_0(v_x \sin\theta_0 - v_y \cos\theta_0)}{r_0}\eta \quad (14)$$

$$R_{Rx^k}(\eta) \cong r_0 + v_r\eta + v_p^2\frac{\eta^2}{2r_0} - \left(kd + \frac{d}{2}\right)\sin\theta_0 + \left(kd + \frac{d}{2}\right)\frac{\cos\theta_0 v_p}{r_0}\eta \quad (15)$$

$$\Delta R_{Tx-b}(\eta) = \sqrt{(x_T - x)^2 + (y_T - y)^2 + z_T^2} - \sqrt{x_T^2 + y_T^2 + z_T^2} \cong -\frac{x_T x + y_T y}{\sqrt{x_T^2 + y_T^2 + z_T^2}} = \frac{x_T(r_0 \cos\theta_0 + v_x \eta) + y_T(r_0 \sin\theta_0 + v_y \eta)}{\sqrt{x_T^2 + y_T^2 + z_T^2}} \quad (16)$$

$$\Delta R_{Tx-b}(\eta) \cong -r_0 \cos\psi_T(\eta) \cdot \cos(\theta_T(\eta) - \theta_0) - \cos\psi_T(\eta) \cdot \left(v_r \cos(\theta_T(\eta) - \theta_0) - v_p \sin(\theta_T(\eta) - \theta_0)\right) \cdot \eta \quad (17)$$

$$\Delta R_{Tx-b}(\eta) \cong -r_0 \cos\psi_{T_0} \cos(\theta_{T_0} - \theta_0) + r_0 \cos\psi_{T_0} \sin(\theta_{T_0} - \theta_0) \cdot \dot\theta_T\eta + r_0 \sin\psi_{T_0}\cos(\theta_{T_0} - \theta_0)\dot\psi_T \cdot \eta +$$

$$-\cos\psi_{T_0}\left(v_r \cos(\theta_{T_0} - \theta_0) - v_p \sin(\theta_{T_0} - \theta_0)\right) \cdot \eta \quad (18)$$

geometry $R_{Tx}(\eta) \gg R_{Rx^k}(\eta)$, $\Delta R_{Tx-b}(\eta)$ can be expanded in Taylor series around the R$_X$ position arresting the series to the first order: (16) shown bottom of previous page.

Recalling that $\theta_T(\eta)$ and $\psi_T(\eta)$ are the satellite aspect and elevation angles of the satellite [see Fig. 2(b)], both possibly changing with time, (16) can be rearranged as (17) shown bottom of previous page.

Further, $\theta_T(\eta)$ and $\psi_T(\eta)$ can be expanded in series as a function of the temporal variable. In this case, the series is arrested to the first order, namely $\theta_T(\eta) \cong \theta_{T_0} + \dot\theta_T \cdot \eta$ and $\psi_T(\eta) \cong \psi_{T_0} + \dot\psi_T \cdot \eta$, since the variation of the satellite aspect and elevation is limited (or even null in the case of geostationary transmitters) due to the high satellite altitude. Thus, we have (18) as shown bottom of previous page.

Finally, from (15) and (18), the bistatic range for the kth antenna element can be written as (19) shown bottom of this page. Therefore: (20) as shown bottom of this page.

It is apparent from (20) that the DFR has a constant value during the whole T_a, which is independent of both spatial and temporal variables k and η. In contrast, the initial phase depends on k, so that signals received at the different antenna elements have a relative phase shift. Moreover, the DC values clearly depends on the antenna element k, so that the bistatic Doppler frequency changes with the antenna element inside the array. This latter consideration shows that the coherent integration of the signals received at the K antenna elements requires more than a constant rephasing before the coherent sum.

It must also be noticed that the linear frequency modulation of the chirp signals implies that the Doppler frequency changes with time. Therefore, different values of the average DC are observed at the N successive temporal frames; namely, the bistatic Doppler centroid is both function of the spatial index, k, and temporal frame index, n. This is easily observed by writing (19) as a function of the temporal variable η' spanning the individual frame as (21) shown bottom of this page.

$$R_k(\eta) \cong r_0\left(1 - \cos\psi_{T_0}\cos(\theta_{T_0} - \theta_0)\right) - \left(kd + \tfrac{d}{2}\right)\sin\theta_0 + \left[v_r + \left(kd + \tfrac{d}{2}\right)\frac{\cos\theta_0\, v_p}{r_0} + r_0\cos\psi_{T_0}\sin(\theta_{T_0} - \theta_0)\cdot\dot\theta_T + \right.$$
$$\left. + r_0\sin\psi_{T_0}\cos(\theta_{T_0} - \theta_0)\cdot\dot\psi_T - \cos\psi_{T_0}\cdot\left(v_r\cos(\theta_{T_0} - \theta_0) - v_p\sin(\theta_{T_0} - \theta_0)\right)\right]\cdot\eta + v_p^2\frac{\eta^2}{2r_0} \tag{19}$$

$$\begin{cases} R_k^0 \cong r_0\left(1 - \cos\psi_{T_0}\cos(\theta_{T_0} - \theta_0)\right) - \left(kd + \tfrac{d}{2}\right)\sin\theta_0 \\[2mm] \bar{f}_k^{dc} = -\frac{1}{\lambda}\left(\begin{array}{c} v_r + \left(kd + \tfrac{d}{2}\right)\frac{\cos\theta_0\, v_p}{r_0} + r_0\cos\psi_{T_0}\sin(\theta_{T_0} - \theta_0)\cdot\dot\theta_T + \\[2mm] + r_0\sin\psi_{T_0}\cos(\theta_{T_0} - \theta_0)\cdot\dot\psi_T - \cos\psi_{T_0}\cdot\left(v_r\cos(\theta_{T_0} - \theta_0) - v_p\sin(\theta_{T_0} - \theta_0)\right) \end{array} \right) \\[2mm] \bar{f}_k^{dr} = -\frac{1}{\lambda}\frac{v_p^2}{r_0} = \bar{f}^{dr} \end{cases} \tag{20}$$

$$R_k(\eta' + n\cdot T_{CPI}) \cong r_0\left(1 - \cos\psi_{T_0}\cos(\theta_{T_0} - \theta_0)\right) - \left(kd + \tfrac{d}{2}\right)\sin\theta_0 + \left[v_r + \left(kd + \tfrac{d}{2}\right)\frac{\cos\theta_0\, v_p}{r_0} + \right.$$
$$+ r_0\cos\psi_{T_0}\sin(\theta_{T_0} - \theta_0)\cdot\dot\theta_T + r_0\sin\psi_{T_0}\cos(\theta_{T_0} - \theta_0)\cdot\dot\psi_T - \cos\psi_{T_0}\cdot$$
$$\left.\left(v_r\cos(\theta_{T_0} - \theta_0) - v_p\sin(\theta_{T_0} - \theta_0)\right)\right]\cdot(\eta' + n\cdot T_{CPI}) + v_p^2\frac{(\eta' + n\cdot T_{CPI})^2}{2r_0} \tag{21}$$

$$R_n = r_0\left(1 - \cos\psi_{T_0}\cos(\theta_{T_0} - \theta_0)\right) + \left[v_r + r_0\left(\cos\psi_{T_0}\sin(\theta_{T_0} - \theta_0)\right)\dot\theta_T + \sin\psi_{T_0}\cos(\theta_{T_0} - \theta_0)\dot\psi_T + \right.$$
$$\left. - \cos\psi_{T_0}\left(v_r\cos(\theta_{T_0} - \theta_0) - v_p\sin(\theta_{T_0} - \theta_0)\right)\right]\cdot n\, T_{CPI} + \frac{v_p^2}{2\,r_0}n^2\, T_{CPI}^2 \tag{22}$$

$$R_k(\eta' + n\cdot T_{CPI}) \cong R_n - \left(kd + \tfrac{d}{2}\right)\left[\sin\theta_0 - \frac{v_p\cos\theta_0}{r_0}n\, T_{CPI}\right] + \left[v_r + \left(kd + \tfrac{d}{2}\right)\frac{v_p\cos\theta_0}{r_0} + \right.$$
$$+ r_0\left(\cos\psi_{T_0}\sin(\theta_{T_0} - \theta_0)\right)\dot\theta_T + \sin\psi_{T_0}\cos(\theta_{T_0} - \theta_0)\dot\psi_T - \cos\psi_{T_0}\left(v_r\cos(\theta_{T_0} - \theta_0) - v_p\sin(\theta_{T_0} - \theta_0)\right) +$$
$$\left. + v_p^2\frac{T_{CPI}}{r_0}n\right]\eta' + v_p^2\frac{\eta'^2}{2r_0} \tag{23}$$

$$\bar{f}_{k,n}^{dc} = -\frac{1}{\lambda}\left[v_r + \left(kd + \tfrac{d}{2}\right)\frac{v_p\cos\theta_0}{r_0} + r_0\left(\cos\psi_{T_0}\sin(\theta_{T_0} - \theta_0)\right)\dot\theta_T + \sin\psi_{T_0}\cos(\theta_{T_0} - \theta_0)\dot\psi_T + \right.$$
$$\left. - \cos\psi_{T_0}\left(v_r\cos(\theta_{T_0} - \theta_0) - v_p\sin(\theta_{T_0} - \theta_0)\right) + v_p^2\frac{T_{CPI}}{r_0}n\right] \tag{24}$$

$$\begin{cases} \tan\bar\alpha = \frac{T_{CPI}}{PRF}\bar{f}^{dr} = -\frac{T_{CPI}}{PRF}\frac{v_p^2}{\lambda\, r_0} \\[3mm] \bar{f}_\alpha = \bar{f}_{k,n}^{dc}\cos\bar\alpha = \\[3mm] \quad = -\dfrac{v_r + \left(kd + \tfrac{d}{2}\right)\frac{v_p\cos\theta_0}{r_0} + r_0\left(\cos\psi_{T_0}\sin(\theta_{T_0} - \theta_0)\right)\dot\theta_T + \sin\psi_{T_0}\cos(\theta_{T_0} - \theta_0)\dot\psi_T - \cos\psi_{T_0}\left(v_r\cos(\theta_{T_0} - \theta_0) - v_p\sin(\theta_{T_0} - \theta_0)\right) + v_p^2\frac{T_{CPI}}{r_0}n}{\lambda\sqrt{1 + \left(\frac{T_{CPI}}{PRF}\frac{v_p^2}{\lambda r_0}\right)^2}} \end{cases} \tag{25}$$

By setting (22), this yields (23), as shown bottom of previous page. Therefore, the Doppler frequency measured by the kth receiving antenna element at the nth frame time is given by (24), implying that the output of the FrFT is expected to provide a peak at (25), as shown bottom of previous page.

This means that the K rotated frequency-angle maps at the different antenna elements have the peak at the same angle but at different values of $\bar{f}_\alpha$. The shift in the value of $\bar{f}_\alpha$ between the kth antenna element and the reference position (hereafter referred to as spatial f_α-shift) is given by

$$\Delta \bar{f}_\alpha^k = -\frac{1}{\lambda}\left(kd + \frac{d}{2}\right) \frac{v_p \cos \theta_0}{r_0} \Big/ \sqrt{1 + \left(\frac{T_{CPI}}{PRF} \frac{v_p^2}{\lambda r_0}\right)^2} \quad (26)$$

By inspecting (26), it is easy to see that $\Delta \bar{f}_\alpha^k$ depends on the target Doppler rate. Recalling the relationship between the target DFR and the optimum rotation angle of the FrFT in (25), we have $|v_p| = \sqrt{-\lambda r_0 \frac{PRF}{T_{CPI}} \tan \bar{\alpha}}$. Therefore, for a generic DFR (i.e., for a generic rotation angle), we obtain

$$\Delta f_\alpha^k = -sign[v_p]\left(kd + \frac{d}{2}\right) \cos \theta_0 \sqrt{-\frac{\sin 2\alpha}{2\lambda r_0} \frac{PRF}{T_{CPI}}} \quad (27)$$

From the above equation, we can observe that the spatial f_α-shift depends on the rotation angle corresponding to the DFR of the target as well as its distance from the array, namely in the (f_α, α) plane a shift in f_α that depends on α. However, inspecting (27) we can note that Δf_α^k also depends on the unknown target DOA. Even though the search procedure to perform the estimation of the DOA (addressed in the following) may include also this frequency alignment step, taking into account the relative slow motion of the targets of interest, the dependence of Δf_α^k on θ_0 can be neglected. Specifically, from (24), if $max \left|\left[\left(kd + \frac{d}{2}\right)(1 - \cos \theta_0)v_p\right] \Big/ \lambda r_0\right| < 1/T_{CPI}$, the residual frequency offset uncompensated by neglecting the effect of the DOA will be certainly confined in the DC resolution cell. Therefore, Δf_α^k can be approximated as

$$\Delta f_\alpha^k \approx -sign[v_p]\left(kd + \frac{d}{2}\right) \sqrt{-\frac{\sin 2\alpha}{2\lambda r_0} \frac{PRF}{T_{CPI}}} \quad (28)$$

While the coherent time integration is nicely performed by the FrFT for each receiving antenna element, to obtain the desired space-time coherent integration of the K maps, these must be coherently combined. To this purpose, we need to keep into account the expected shift of the peak in the K maps, so that we coherently integrate the appropriate (f_α, α) cell, where most of the target energy locates, and we want to add coherently the values in these (f_α, α) locations (namely on a pixel-by pixel basis) over the spatial dimension k to increase the target energy.

It is to be noticed that the compensation of the rotated frequency shift change among antenna elements also depends on the sign of the parallel velocity, which might be unknown. In this case, also this sign must be estimated from the collected signals, by attempting the compensation with both possible

values and comparing the two resulting peaks.

According to the phased array theory [37], the K maps can be coherently combined accounting for a set of delay phase terms (i.e., the steering vector) that lineup the returns from a given direction. If such a direction coincides with the actual target DOA, the maximum gain will be obtained. Therefore, the integration of the K maps of the individual frames can be performed after appropriate phase compensation, i.e., from (23), by multiplying the kth map for the term:

$$\phi_{k,n} = exp\left\{-j\frac{2\pi}{\lambda}\left(kd + \frac{d}{2}\right)\left[\sin \theta_0 - \frac{v_p T_{CPI}}{r_0} n \cdot \cos \theta_0\right]\right\} (29)$$

This clearly depends on n, so that a different compensation must be applied to each frame. Moreover, we can observe that the phase terms in (29) depend on the target parallel velocity, and therefore, from (25), on the optimum rotation angle. After simple manipulations, for a target with generic DFR, we obtain

$$\phi_{k,n} = \exp\left\{-j\frac{2\pi}{\lambda}\left(kd + \frac{d}{2}\right)\left[\sin \theta_0 - sign(v_p)\, n \cdot \cos \theta_0 \cdot \sqrt{-\frac{\lambda}{r_0} PRF\, T_{CPI} \tan \alpha}\right]\right\} \quad (30)$$

From the above equation, we can observe that the steering vector depends on the rotation angle corresponding to the DFR of the target as well as its distance from the array. However, since θ_0 is unknown, a search procedure has to be carried out: (i) the angle spanning the receiving antenna beamwidth Θ is quantized with a step equal to a fraction of the expected angular resolution $\left(\frac{\Theta}{K}\right)$; then, (ii) for each value of θ under test, a different integrated map $S_n(f_\alpha, \alpha; \theta)$ is obtained as

$$S_n(f_\alpha, \alpha; \theta) = \frac{1}{K}\sum_{k=-\frac{K}{2}}^{\frac{K}{2}-1} S_{k,n}(f_\alpha + \Delta f_\alpha^k, \alpha) \cdot$$
$$\exp\left\{-j\frac{2\pi}{\lambda}\left(kd + \frac{d}{2}\right) \cdot \left[\sin \theta - sign(v_p)\, n \cos \theta \cdot \sqrt{-\frac{\lambda}{r_0} PRF\, T_{CPI} \tan \alpha)}\right]\right\} \quad (31)$$

by varying the phase terms in the (f_α, α) plane and (iii) the space-time coherent integration is provided by the maximum value, which is obtained for the value of θ corresponding to the actual target DOA. Clearly, while looking for the peak in the FrFT maps provides a search in the 2D plane of the DC-DFR values and performs the temporal coherent integration, the selection of the combination of the K maps providing the maximum value extends the search to 3D and provides the final space-time coherent integration. As for the frequency shift compensation, when the sign of v_p is unknown both possible values are attempted and the corresponding outputs compared.

C. Frame to frame processing

Because of its motion, the target locates in different positions when observed in different frames. The KT accomplished at the pre-processing stage allows correcting the range migration for the entire dwell. Nevertheless, the target motion still implies Doppler migration. Consequently, even though the compensation of the spatial f_α-shift allows having the target energy located onto the same f_α position for the K maps

pertaining to the individual frames, the f_α location (namely, the DC) of the target energy will be different frame by frame.

Let Δf^n be the shift in DC position measured at the nth frame interval with respect to the reference instant. Such a shift depends on the different positions of the target when observed at different time instants, therefore we refer to it as to temporal DC-shift. From (24), we have the temporal DC-shift as:

$$\Delta \bar{f}^n = -v_p^2 \frac{T_{CPI}}{\lambda r_0} n = \bar{f}^{dr} T_{CPI} n = PRF \ tan \ \bar{\alpha} \ n \quad (32)$$

and therefore, for the generic DFR, in the (f_α, α) plane a temporal f_α-shift equal to

$$\Delta f_\alpha^n = PRF \ sin \ \alpha \ n \quad (33)$$

To perform the incoherent integration, we need to compensate for the displacement of the DC (namely of f_α) from frame to frame. Therefore, the N maps pertaining the tested θ are non-coherently combined to obtain the final integrated map as:

$$\boldsymbol{S}_{total}(f_\alpha, \alpha; \theta) = \frac{1}{N} \sum_{n=-\frac{N-1}{2}}^{\frac{N-1}{2}} |\boldsymbol{S}_n(f_\alpha + \Delta f_\alpha^n, \alpha; \theta)|^2 \quad (34)$$

Thanks to the effect of both coherent and incoherent integration, the equivalent signal to disturbance ratio is largely increased and the presence of a mover can be reliably detected in the $\boldsymbol{S}_{total}(f_\alpha, \alpha; \theta)$ map corresponding to its actual DOA. As is apparent, this jointly provides the target detection and the target DOA estimation.

A few considerations apply to the implementation of the total incoherent sum. As is apparent, the final sum can be rewritten as

$$\boldsymbol{S}_{total}(f_\alpha, \alpha; \theta) = \frac{1}{N} \sum_{n=-\frac{N-1}{2}}^{\frac{N-1}{2}} |\boldsymbol{S}_n(f_\alpha + \Delta f_\alpha^n, \alpha; \theta)|^2 =$$

$$= \frac{1}{N} \sum_{n=-\frac{N-1}{2}}^{\frac{N-1}{2}} \left| \frac{1}{K} \sum_{k=-\frac{K}{2}}^{\frac{K}{2}-1} \boldsymbol{S}_{k,n}(f_\alpha + \Delta f_\alpha^k + \Delta f_\alpha^n, \alpha) \cdot \phi_{k,n}(\theta) \right|^2 \quad (35)$$

and, by defining the realigned rotated frequency-angle maps

$$\boldsymbol{S}_{k,n}^{al}(f_\alpha, \alpha) = \boldsymbol{S}_{k,n}(f_\alpha + \Delta f_\alpha^k + \Delta f_\alpha^n, \alpha) \quad (36)$$

the total sum is given by:

$$\boldsymbol{S}_{total}(f_\alpha, \alpha; \theta) = \frac{1}{N} \sum_{n=-\frac{N-1}{2}}^{\frac{N-1}{2}} \left| \frac{1}{K} \sum_{k=-\frac{K}{2}}^{\frac{K}{2}-1} \boldsymbol{S}_{k,n}^{al}(f_\alpha, \alpha) \cdot \phi_{k,n}(\theta) \right|^2 \quad (37)$$

The main problem is related with the evaluation of the realigned maps $\boldsymbol{S}_{k,n}^{al}(f_\alpha, \alpha)$. This is the FrFT of the nth frame received at the kth receiving antenna, evaluated at the rotated frequency $f_\alpha + \Delta f_\alpha^k + \Delta f_\alpha^n = f_\alpha \pm \frac{2k+1}{2} cos \ \theta \sqrt{-\frac{sin \ 2\alpha}{2\lambda r_0} \frac{PRF}{T_{CPI}}} +$ PRF $sin \ \alpha \ n$, which is simplified into $f_\alpha + \Delta f_\alpha^k + \Delta f_\alpha^n = f_\alpha \pm \frac{2k+1}{2} d \sqrt{-\frac{sin \ 2\alpha}{2\lambda r_0} \frac{PRF}{T_{CPI}}} +$ PRF $sin \ \alpha \ n$ when the effect of the DOA is negligible.

Two alternative strategies can be applied to perform the map realignment:

(a) Evaluate the FrFT $\boldsymbol{S}_{k,n}(f_\alpha, \alpha)$ of the signal received at each of the N frames and of the K antenna elements; then obtain the shifted value by resorting to an interpolation along the f_α axis to evaluate its value at frequency $f_\alpha \pm \left(kd + \frac{d}{2}\right) cos \ \theta \sqrt{-\frac{sin \ 2\alpha}{2\lambda r_0} \frac{PRF}{T_{CPI}}} +$ PRF $sin \ \alpha \ n$.

(b) Apply a phase ramp in the u domain with slope $\pm \left(kd + \frac{d}{2}\right) cos \ \theta \sqrt{-\frac{sin \ 2\alpha}{2\lambda r_0} \frac{PRF}{T_{CPI}}} +$ PRF $sin \ \alpha \ n$, according to (27) and (33) before evaluating the FT over u so that the shifted FrFT is directly obtained after the FT.

Solution (a) requires an interpolation along the f_α dimension that is dependent on the value of α, namely a different shift is applied for different values of α. The accuracy of the required interpolation depends on the acceptable loss in the maps combination. As apparent, if the exact shift is to be considered, as a function of θ, this approach allows the FrFT to be evaluated only once and a different interpolation to be performed for different values of θ. Obviously a single interpolation is required for each frame and antenna element if the shift can be approximated as $\pm \left(kd + \frac{d}{2}\right) \sqrt{-\frac{sin \ 2\alpha}{2\lambda r_0} \frac{PRF}{T_{CPI}}} +$ PRF $sin \ \alpha \ n$.

Solution (b) implies a phase shift that is dependent on the value of α, namely a different shift is applied for different values of α. Taking into account both the spatial and temporal shifts, the realigned maps can be obtained by evaluating directly

$$\boldsymbol{S}_{k,n}^{al}(f_\alpha, \alpha) = \int_{-\infty}^{+\infty} s_\alpha(u) \cdot \exp\{-j2\pi(f_\alpha - \Delta f_\alpha^k - \Delta f_\alpha^n)u\} \, du \quad (38)$$

We notice that the FT with a constant phase shift can also be interpreted as a very specific case of Chirp Zeta Transform (CZT). When $\Delta f_\alpha^k + \Delta f_\alpha^n$ can be approximated as $\pm \left(kd + \frac{d}{2}\right) \sqrt{\frac{sin \ 2\alpha}{2\lambda r_0} \frac{PRF}{T_{CPI}}} +$ PRF $sin \ \alpha \ n$, this is certainly a computationally convenient implementation of the realignment. In contrast, when the variation with $cos \ \theta$ cannot be neglected, the evaluation of the realigned maps for the different values of θ requires repeating the FT over u.

Independent of the selected solution, three considerations are in order:

(i) It should be pointed out that the selection of the rotated frequency shift (27)/(28), or of the equivalent slope of the phase ramp to be applied, and of the phase term (30) to carry out the space-time coherent processing, requires the knowledge of the target distance from the array, r_0. So far, we assumed as known this value, because the processing is separately applied to each range cell composing the surveillance area. Nevertheless, the range value associated to the generic cell under test represents the differential bistatic value measured by the system, and therefore it differs from r_0. However, from (23), we can observe that the relationship between the target to receiver distance r_0 and the differential bistatic range depends on the satellite position with respect to the receiver and on the target DOA. In particular, from (23) the bistatic range measured at the nth
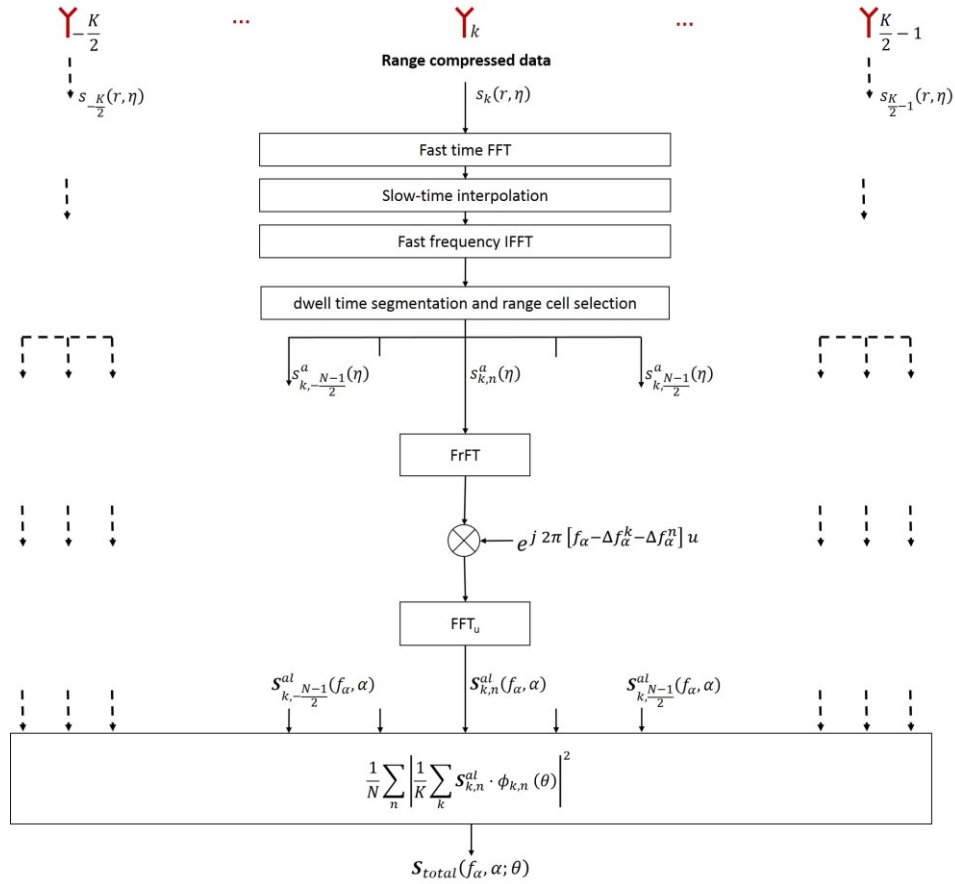
Fig. 5. Proposed processing scheme.

frame interval is given by $R_n - \left(kd + \frac{d}{2}\right) \cdot [\sin \theta_0 - \frac{v_p \cos \theta_0}{r_0} n T_{CPI})]$ thus it depends on both the considered frame and antenna element. However taking into account the keystone reformatting at the pre-processing stage, which compensates the target range migration over the different frames aligning all contributions in the same range bin, and observing that the range variations due to the different antenna element positions are much less than the range resolution cell, (9), the above dependence can be neglected. Considering the transmitter to target distance much higher than the target to receiver distance, the relation between r_0 and the measured range value R_0 (i.e., the value corresponding to the range cell under test) can be written as

$$r_0 = \frac{R_0}{(1 - \cos \psi_{T_0} \cos(\theta_{T_0} - \theta_0))} \qquad (39)$$

Therefore, a DOA-dependent scale factor according to (39) can be considered to compensate the difference between the measured bistatic range and the required monostatic value for the correct application of (27) or (28) and (30). However, it is easy to see that:

- for targets at relatively short ranges, $R_{Tx}(\eta) \approx R_b(\eta)$, thus the measured bistatic range is very close to the target to array distance, whereas the same consideration does not apply for targets quite far from the receiver;
- the difference of the DC measured from the different

antennas depends on the different angles under which the target is observed: when the target is sufficiently far from the array, it offers approximately the same DOA to each element of the array.

On this basis $r_0 \cong R_0$ could be considered in (28), namely the DOA-dependent correction factor could be neglected in the maps realignment. With regard to the rephasing of the individual maps for the DOA estimation procedure, (30), this already requires a search procedure over the different possible target DOAs. Therefore, the DOA-dependent correction factor can be easily taken into account in the K maps coherent summation (31).

(ii) The application of the rotated frequency shift, or the equivalent slope of the phase ramp to be applied, which depends on the value of α shows that the selected operation in the (u, α) plane provided by the FrFT is the most natural domain to perform the integration, since it allows to easily apply the desired phase compensations by operating only on matrix rows or columns.

(iii) Because the selection of the rotated frequency shift slope depends on the value of the angle α, the application of the rotated frequency shifts results not only in a translation of the spectrum of the signal in the (f_α, α) plane, but also in a rotation. The entity of such a rotation depends on both k and n, so that the spectrums of the KN signals (i.e., $\left|S_{k,n}^{al}\right|^2$) are differently rotated around the reference $\left(\bar{f}_\alpha, \bar{\alpha}\right)$ position. Therefore, the

summations of the $\boldsymbol{S}_{k,n}^{al}$ maps in (37) provide also an improvement of the concentration of the signal energy, namely a narrower peak, in the final integrated map $\boldsymbol{S}_{total}$.

The complete processing scheme obtained by selecting solution (b), under the assumption that an approximate rotated frequency shift (independent of θ) is enough, is reported in Fig. 5. As is apparent the application of the linear phase terms to compensate spatial and temporal rotated frequency shifts, inside the FrFT block, allows to appropriately realigning the KN (f_α, α) maps so that both coherent space-time integration and incoherent frame-to-frame integration can be applied on a pixel-by-pixel basis.

As a final comment on the proposed processing scheme in Fig. 5, we observe explicitly that the temporal DC-shift depends on the square of the parallel velocity. Therefore, the alignment of the maps pertaining the different frames can be accomplished by making use of solution strategy (a) or (b) independently from the sign of the parallel velocity. In contrast, the space-time coherent processing depends on the sign of the velocity, both for the compensation of the spatial f_α-shift, (28), and for the rephasing of the maps, (30). Obviously, since this information is generally unknown, both the compensations pertaining to a positive or a negative parallel velocity have to be tested, with the maximum integration gain achieved for the actual sign. Therefore, the branches of the scheme of Fig. 5 corresponding to the space-time compensation are duplicated. Thus, the procedure is potentially able to recover not only the absolute parallel speed, as achieved with the single receiver scheme in [36], but also the direction of the motion.

IV. PERFORMANCE ANALYSIS

In this section, simulation results are presented to illustrate the proposed technique and verify its effectiveness in detecting and identifying the direction-of-arrival of ship targets. In the simulated scenario we consider an array receiver composed by K = 14 elements with inter-element distance $d = 2\lambda$. This entails grating lobes at $\pm 30°$ of steering direction [37], which is supposed to be sufficiently larger than the antenna beamwidth.

A navigation satellite is considered as transmitter of opportunity. The reason of this choice is that this represents maybe the worst case for the system under consideration in terms of power budget. Indeed, GNSS are very low EIRP sources, with a power density near the surface of the Earth down to -135 dBW/m² [24], thus requiring dwell times in the order of tens of seconds to reach acceptable level of signal to disturbance ratios [27][28]. The parameters of the simulations are listed in Table I.

First, for sake of illustration, we provide simulated results in noise-free background. We consider a ship target with position $\boldsymbol{p}_0 = [1300, 100]$ m at the reference instant, which corresponds to a DOA $\theta_0 = 4.40°$, and moving with velocity $\boldsymbol{v} = [7.07, 7.07]$ kn. During the dwell time $T_a = 62$ s, signal reflections are collected by the array, while the direct signal recorded by the reference channel is exploited to perform the signal synchronization with equivalent $PRF = 1$ kHz [18],

TABLE I. SIMULATION PARAMETERS

Transmitter	
Satellite	GPS
Carrier frequency	1575.42 MHz
Signal bandwidth (chip-rate L1 channel)	1.023 MHz
Power density over Earth 'surface	-135 dBW/m²
Receiver	
Number of elements	14
Inter-element distance	38 cm
Beamwidth	30°
Effective area of each element	0.14 m²

[26]. By cross-correlation of the reference signal with the signal received by each element of array, K range-compressed&slow-time matrices are obtained. Keystone reformatting is applied, thus compensating the RCM for the entire dwell time. Then, data segmentation is performed with frame duration $T_{CPI} = 2$ s, resulting in N = 31 frames, and the multiple frames are processed making use of the processing in Fig. 5. Fig. 6 shows the results obtained at different steps of the processing chain, as described ahead.

First, we focus on the space-time coherent integration for an individual frame. Let us consider the reference frame $n = 0$ and suppose we have selected the range cell containing the target. By means of FrFT, K (f_α, α) maps can be obtained. Fig. 6(a) shows the map in the DC-DFR domain obtained for the reference antenna of the array. We can observe that the target energy is concentrated along a slice in the Doppler frequency direction corresponding to -16.658 Hz, with a peak value around the DFR -0.045 Hz/s. Let us consider for this frame the antenna elements at the edges of the array, i.e. $k = -\frac{K}{2}$ and $k = \frac{K}{2} - 1$. Such antennas measure target Doppler frequencies different from the measurement of the reference antenna. In particular, we found $f_{-\frac{K}{2}}^{dc} = -16.690$ Hz and $f_{\frac{K}{2}-1}^{dc} = -16.626$ Hz, whereas the maximum difference in Doppler rate could be show to be about 0.0001 Hz/s, therefore much lower than $\frac{1}{T_{CPI}^2}$ thus in accordance with our hypothesis [see (4)]. Therefore, in the K maps, target energy occupies slices centered on the same angle but on different f_α positions. To assure the alignment of the maps pertaining to different antennas, a phase ramp with slope according to the rotated frequency shift in (28) for each angle can be applied in the (u, α) plane. It is worth to notice that for this target the maximum variation of the DC measured by the array is about 0.035 Hz, therefore lower than the Doppler resolution cell (equal to $\frac{1}{T_{CPI}} = 0.5$ Hz). In such conditions, the alignment in the frequency domain of the elements of the array has a limited impact on the system performance and ultimately it could be neglected here. In the following, we will consider a different scenario where such an alignment is mandatory to collect correctly the signal energy over the array.

At this point, the K maps can be coherently integrated accounting for a phase term according to (30) and the obtained DC-DFR map pertaining to the actual DOA is shown in Fig.
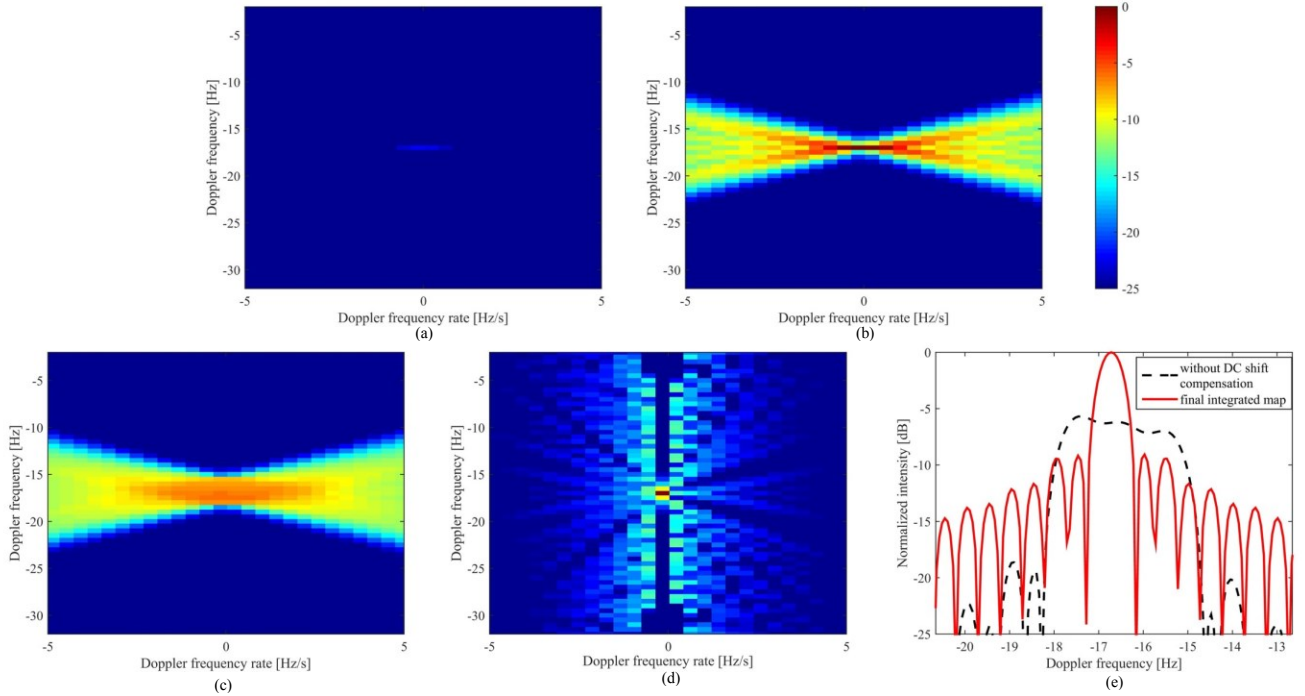
Fig. 6. Simulated results in noise-free background - a) Single-antenna single frame DC-DFR map, b) multi-antenna single frame, c) multi-antenna multi-frame without temporal f_α-shift compensation, d) multi-antenna multi-frame, e) comparison Doppler frequency cut for the multi-antenna multi-frame case.
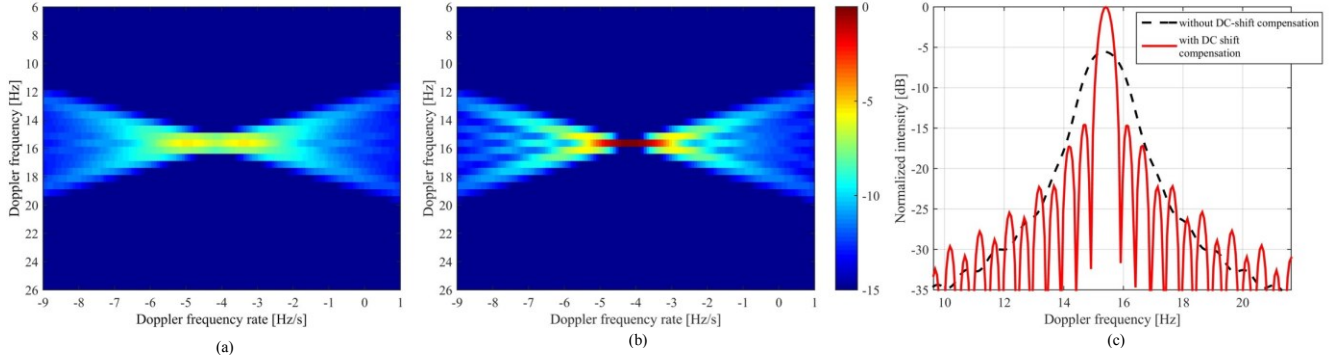

Fig. 7. Single frame results for a fast and close moving target – integration of the multi-frame without (a) and with (b) f_α-shift compensation and Doppler frequency cross-sections (c).

6(b): the improvement in signal energy is apparent and specifically it is equal to 22.9 dB; since K = 14, it is in line with the theoretical expectation.

Let us now consider the integration over the multiple frames. By the compensation of the spatial f_α-shift, the K maps concerning the nth frame are co-registered, namely the peaks of the signal energy occupy the same (f_α, α) position. Nevertheless, Doppler migration still exists among the different frames. In the considered case study, the target DC position is -15.108 Hz for the first processed frame $n = -(N-1)/2$, whereas in the last frame $n = (N-1)/2$ it is -17.839 Hz. Therefore, a spread of the target energy will occur if the integration over the long dwell time is performed without any compensation of such a shift. For illustrative purposes only, we show in Fig. 6(c) the final integrated DC-DFR map that would be obtained if the N single-frame maps were non-coherently integrated without compensating the temporal f_α-shift. We can observe a blurring effect due to the uncompensated Doppler migration among the frames. By multiplying the data in the (u, α) domain for a phase ramp with slope according to (33), the temporal f_α-shift among the frames can be adaptively compensated by varying α in the (u, α) plane. Fig. 6(d) shows the final integrated map, where we can observe that the signal energy has been well concentrated in the DC-DFR domain. Fig. 6(e) compares the Doppler frequency cross sections around the actual DFR for the multi-frame integration non-compensating (black dotted line) or compensating (red full line) the temporal f_α-shift among the frames. From the figure, it is easy observing how the correct compensation of the target Doppler migration during the dwell time provided a gain of about 5 dB.

As mentioned, in the previous case study although the different elements of the array measure different DC, the maximum variation was lower than a fraction of the Doppler resolution cell, thus making superfluous the frequency alignment of the data pertaining different array elements in the individual frame. However, for targets moving with higher
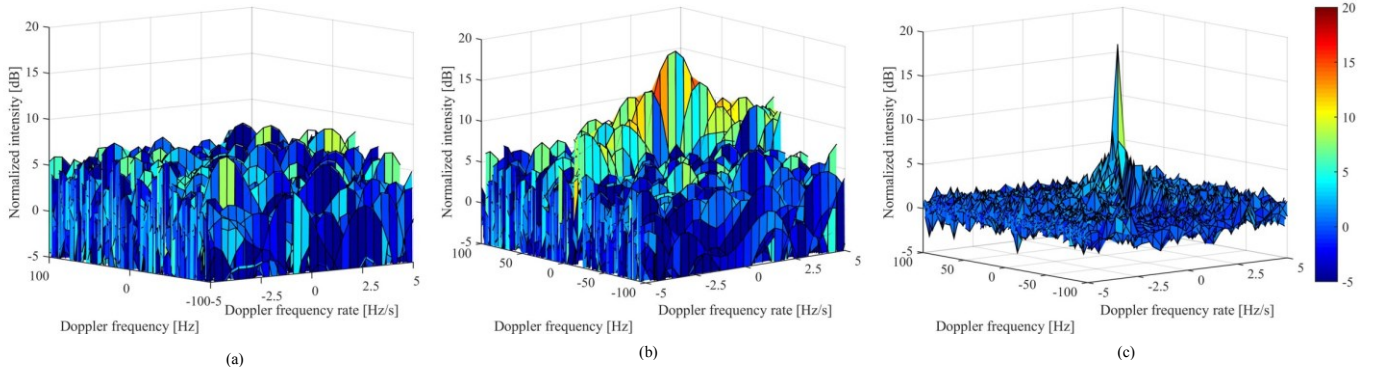
Fig. 8. Simulated results in noise background – a) single antenna and single frame, b) multi-antenna and single frame, c) multi-antenna and multi-frame.

speeds and/or at closer ranges the compensation of the spatial f_α-shift is a mandatory step. Let us consider a second target in the field of view of the radar antenna with position $\boldsymbol{p}_0 = [299,23]$ m at the reference time, which was moving with very high velocity $V = 30$ kn parallel to the array. In such conditions, at the reference frame the elements at the edges of the array measure $f_{-\frac{K}{2}}^{dc} = 14.90$ Hz and $f_{\frac{K}{2}-1}^{dc} = 16.24$ Hz. Therefore, in this case the DC shift over the array is larger than the DC resolution cell and it needs to be compensated (whereas the maximum difference in DFR is around 0.015 Hz/s, therefore still lower than the DFR resolution). Fig. 7(a) shows the DC-DFR map obtained by performing the space-time coherent integration when not any spatial f_α-shift compensation has been carried out. In contrast, the result obtained by applying the spatial f_α-shift compensation procedure driven by the rotation angle of the FrFT in (28) is shown in Fig. 7(b). As it is apparent, the realignment of the K maps enables the correct coherent integration over the array elements, providing a significant integration gain, as can be well observed looking at the comparison of the Doppler frequency cross-sections in Fig. 7(c).

Now, a disturbance background has been also included in the simulation. In particular, we considered the same simulated scenario in Fig. 6 and the target RCS is set equal to 24 dB. As disturbance background, we assume an additive white Gaussian noise occupying the useful signal bandwidth. Assuming a receiver noise figure of 1.5 dB and system losses of 6 dB, the SNR after matched filter in the range-compressed&slow-time domain is about -24 dB.

Fig. 8 shows the obtained results in terms of DC-DFR surfaces, where 0 dB denotes the mean noise power. Fig. 8(a) shows the map concerning the reference antenna and the reference frame, where we can observe that the integration gain provided by the FrFT at the single element-frame level does not suffice to extract the target from the disturbance. Fig. 8(b) shows the result achieved from the coherent integration of the maps pertaining the K antennas in a single frame for the actual DOA in (31). As it is apparent, the coherent integration gain allowed collecting enough signal power to compete with the disturbance. Nevertheless, the strong noise fluctuations still make the detection of the target a challenging task. By carrying
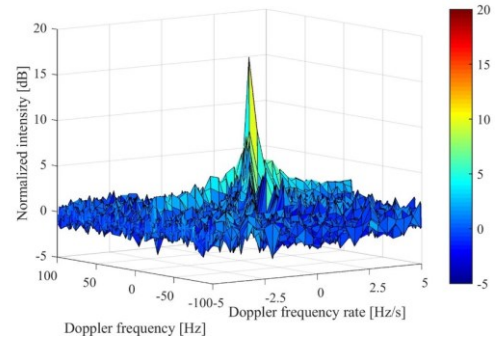

Fig. 9. Final integrated DC-DFR map for the complex target with yaw, pitch and roll motions.

out the non-coherent integration of the multi-frame maps, Fig. 8(c), the disturbance fluctuations are reduced. At the same time, the signal energy is correctly collected over the long dwell. Moreover, we can observe the higher concentration of the energy achieved in the final integrated map in Fig. 8(c), thanks to the rotation of the individual element/frame spectrum resulting from the application of the α-dependent spatial and temporal f_α-shifts: ultimately, a clear and isolated peak is well visible in the final integrated map and therefore the target can be reliably detected.

In order to show results in a more realistic scenario, we removed here the hypothesis of a single point target and we considered a ship with length 30 m and width 6 m composed by 13 dominant scatterers. Moreover, in addition to the translational motion, we considered the ship undergoing rotations induced by the sea waves. The ship rotations are modelled as sinusoidal yaw (amplitude = 0.3°, frequency = 0.07 Hz), pitch (amplitude = 0.3°, frequency = 0.06 Hz) and roll (amplitude = 1.7°, frequency = 0.03 Hz). The remainder parameters of the simulation are as the case study in Fig. 8. Fig. 9 shows the resulting final integrated map. With respect to the ideal case of single point-like target and null rotations, some losses in peak power occurred. Specifically, we found a loss of about 1.6 dB moving from the scenario in Fig. 8 to this more complex one. Such limited losses indicate the robustness of the proposed technique, thus supporting its practical application in real environments.

So far, we considered the coherent summation with the phase terms (30) pertaining for the actual target DOA. Now, we
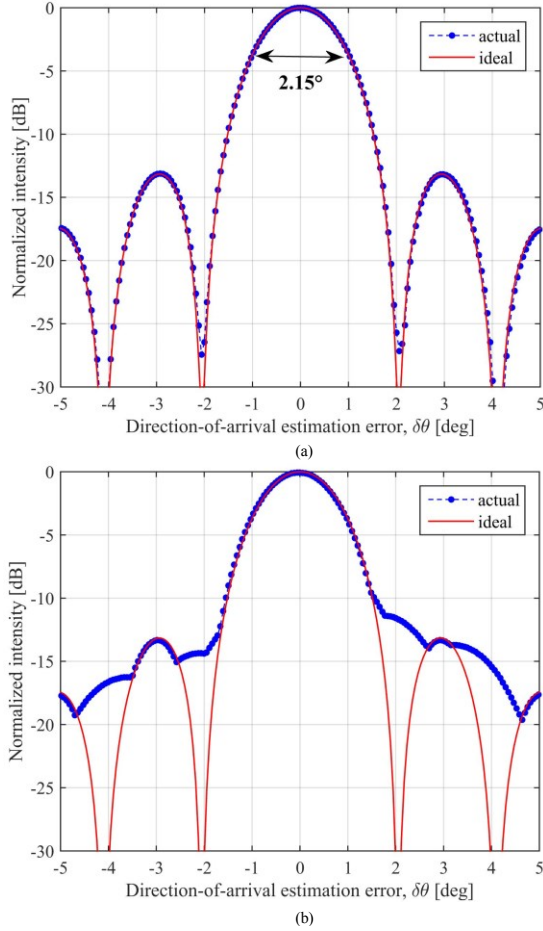
(a)

(b)

Fig. 10. Array pattern for the single frame (a) and the multi-frame (b) cases.

investigate the DOA estimation procedure. The phases of the steering vectors in (30) are composed by two terms: a constant term representing the target DOA at the aperture center θ_0 and an α-dependent offset that takes into account the variation of the target DOA during the long dwell. The latter term can be adaptively compensated by varying its value in each (f_α, α) map, thus an integrated map (37) can be obtained for each tested θ: the estimated DOA $\hat{\theta}_0$ is the achieved by looking for the maximum value among the final integrated maps.

The above procedure has been applied to the same simulated scenario in Fig. 6. Fig. 10 shows the achieved array patterns as a function of the DOA estimation error $\delta\theta = \hat{\theta}_0 - \theta_0$, which has been obtained by storing the peak power of the corresponding integrated map. Fig. 10(a) shows the array pattern obtained when only the reference frame has been considered. Red line represents the ideal case. Because we are not considering any tapering applied to the array, the ideal pattern is a sinc function, centered on $\delta\theta = 0°$, with a mainlobe (at the -4 dB cut) equal to $\Theta/K = 2.14°$. Blue markers represent the estimated points and we can observe a good coincidence with the theoretical pattern (red line). The estimated pattern is centered on $\delta\theta = 0°$ and its beamwidth is 2.15°. Fig. 10(b) shows the results obtained considering the integration of all the frames. We can observe the worsening of the performance with respect to the single frame pattern, due to a partial mismatch
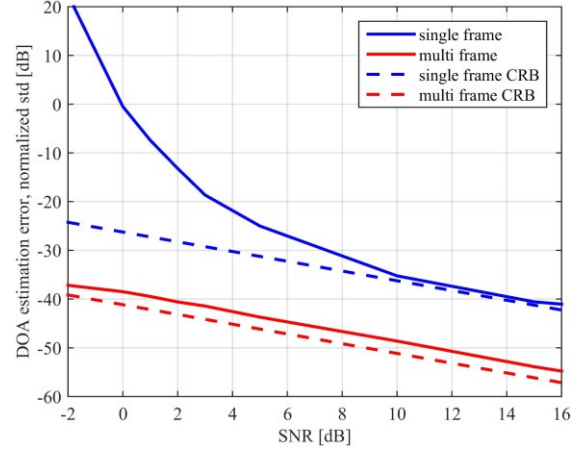

Fig. 11. Normalized standard deviation of the DOA estimation error.

between the considered signal model and the actual conditions. Indeed in the considered scenario, because of the particularly long dwell considered in this simulation (~1 min), the target DFR slightly changes over the different frames (specifically, we found a difference of about 0.0245 Hz/s moving from the first to the last frame considered), thus entailing a worse angular resolution than the theoretical value. Nevertheless, the technique still provides a good capability in estimating the target DOA, with a resolution of about 2.17°. It is also worth to notice that the considered case is particularly unfavorable because of the very long dwell considered. By considering shorter dwell, the variation of the target DFR will be confined in the resolution cell, thus achieving DOA estimation performance closer to the theoretical expectations.

Finally, the DOA estimation performance is investigated. Specifically the theoretical estimation performance is firstly quantified by evaluating the Cramer Rao Bound (CRB). Starting from results in [39], it could be shown that the CRB of the DOA estimation for a single frame is given by

$$\sigma^2_{\theta_{s.f.}} = \frac{6}{K \, SNR \left(\frac{2\pi}{\lambda} d \cos\theta\right)^2 (K^2 - 1)} \tag{40}$$

being SNR the signal-to-noise ratio evaluated at the single (f_α, α) map level. When multiple frames are considered, the evaluation of the CRB is less straightforward, because of the non-coherent integration. As benchmark of the lower bound of the estimation accuracy achievable with the multi-frame processing, we evaluate the CRB in the hypothesis of a full coherent combination of the multi-frame maps, namely by assuming a sensitivity gain equal to N (thus replacing in the above CRB SNR with N·SNR). Theoretical results are then compared to those from a simulated analysis. For the same scenario in Fig. 8, Fig. 11 compares the standard deviation of the DOA estimation error to the corresponding CRB (both normalized to the actual DOA value). Specifically, the dotted lines represent the CRB assuming the estimation realized over a single frame (blue line) or over the multiple frames in the hypothesis of a full coherent combination (red line), whereas the full lines represent the performance of the proposed

technique as evaluated by means of Monte Carlo simulations (10000 independent trials for each tested value of SNR). As it is apparent, in the single frame case the proposed technique reaches performance close to the CRB for SNR of about 10 dB, whereas the same level of performance is reached for significantly lower SNR levels in the case of multiple frames (namely, longer dwell times), thanks to the proper frequency and phase compensation carried out by the proposed technique. Noticeably, the estimation performance achieved with the multiple frames integration is quite close to the benchmark represented by the ideal full coherent processing, thus showing the effectiveness of the proposed long integration time technique for the joint detection and DOA estimation of targets of interest in the considered satellite-based configuration.

V. Conclusions

This paper addressed the detection of surface slow moving targets by means of an array passive radar based on low-EIRP satellite illuminators of opportunity. In addition to the exploitation of long integration times, the use of the receiving array provides both an increase in signal-to-noise ratio and the capability to estimate the target DOA with respect to the receiver. A full processing scheme has been proposed that performs a coherent space-time integration of the signals received at the K antenna elements during frames short enough so that the target behavior can be considered fully correlated, followed by an incoherent frame to frame integration.

The presented analysis illustrated that the DFR is approximately constant over receiving antenna elements and temporal frames, whereas the DC is subject to a shift depending on the antenna element number k and on the frame number n. These shifts are shown to be directly related to the actual DFR and to the bistatic range, therefore by applying a FrFT on each range cell, the shift is only present along the rotated frequency axis. Even more important, the shift depends on the FrFT angle (which is in a monotonic relationship with DFR), so that its compensation is especially natural in the FrFT rotated frequency-angle plane. After FrFT maps compensation, both coherent and incoherent integrations required for target detection are easily performed on a pixel-by-pixel basis, as well as the target DOA estimation, which is intrinsically provided by the integration procedure, as the compensation DOA angle providing the maximum output.

The implementation of the DC shift compensation is discussed with reference to different strategies. Moreover, a few case studies are presented to illustrate the presented analysis of the behavior of the received signals and the effectiveness of the proposed processing technique.

References

[1] H. D. Griffiths and C. J. Baker, "Passive coherent location radar systems. Part 1: Performance prediction," in *IEE Proceedings - Radar, Sonar and Navigation*, vol. 152, no. 3, pp. 153-159, 3 June 2005.

[2] P. E. Howland, D. Maksimiuk and G. Reitsma, "FM radio based bistatic radar," in *IEE Proceedings - Radar, Sonar and Navigation*, vol. 152, no. 3, pp. 107-115, 3 June 2005.

[3] F. Colone, C. Bongioanni, P. Lombardo, "Multifrequency integration in FM radio-based passive bistatic radar. Part I: Target detection," *IEEE Aerospace and Electronic Systems Magazine*, vol. 28, n. 4 April 2013, pp. 28-39.

[4] R. Saini, M. Cherniakov, "DTV signal ambiguity function analysis for radar applications," *IEE Proc. Radar, Sonar and Navigation*, 2005, vol. 152, pp. 133–142.

[5] F. Colone, D. Langellotti, P. Lombardo, "DVB-T Signal Ambiguity Function Control for Passive Radars," *IEEE Trans. on Aerospace and Electronic Systems*, vol. 50, no. 1, pp. 329-347, Jan. 2014.

[6] R. Zemmari, M. Broetje, G. Battistello, U. Nickel, "GSM passive coherent location system: performance prediction and measurement evaluation," *IET Radar, Sonar & Navigation*, vol. 8, no. 2, pp. 94 – 105, Feb. 2014.

[7] F. Colone, K. Woodbridge, H. Guo, D. Mason, C.J. Baker, "Ambiguity Function Analysis of Wireless LAN Transmissions for Passive Radar," *IEEE Trans. on Aerospace and Electronic Systems*, vol. 47, no. 1, pp. 240 – 264, Jan. 2011.

[8] F. Colone, P. Falcone, C. Bongioanni, and P. Lombardo, "WiFi-Based Passive Bistatic Radar: Data Processing Schemes and Experimental Results," IEEE Trans. on Aerospace and Electronic Systems, vol. 48, no. 2, pp. 1061-1079, Apr. 2012.

[9] D. Pastina, F. Colone, T. Martelli, P. Falcone, "Parasitic exploitation of WiFi signals for indoor radar surveillance," *IEEE Trans. Vehicular Tech.*, vol. 64, no. 4, pp. 1401-1415, Apr. 2015.

[10] F. Colone, P. Falcone, P. Lombardo, "Ambiguity Function analysis of WiMAX transmissions for passive radar", *2010 IEEE Radar Conference*, 2010, pp. 689 – 694.

[11] C. Schwark, D. Cristallini, "Advanced multipath clutter cancellation in OFDM-based passive radar systems," *2016 IEEE Radar Conference*, 2016, pp. 1- 4.

[12] M. Cherniakov, D. Nezlin and K. Kubik, "Air target detection via bistatic radar based on LEOs communication signals," in *IEE Proceedings - Radar, Sonar and Navigation*, vol. 149, no. 1, pp. 33-38, Feb 2002.

[13] V. Koch and R. Westphal, "A new approach to a multistatic passive radar sensor for air defense," *Proc. International Radar Conference, Alexandria*, VA, 1995, pp. 22-28.

[14] D. Pastina, M. Sedhei, D. Cristallini, "Geostationary satellite based passive bistatic ISAR for coastal surveillance," *Proc. IEEE Radar Conf.*, Washington, DC, USA, May 2010.

[15] C. Prati, F. Rocca, D. Giancola, and A.M. Guarnieri, "Passive Geosynchronous SAR System Reusing Backscattered Digital Audio Broadcasting Signals," *IEEE Transactions on Geoscience and Remote Sensing*, vol. 36, no. 6, pp. 1973-1976, Nov. 1998.

[16] L. Cazzani, C. Colesanti, D. Leva, et al., "A ground-based parasitic SAR experiment," *IEEE Transactions on Geoscience and Remote Sensing*, vol. 38, no. 5, pp. 2132-2141, Sep. 2000.

[17] M. Cherniakov and T. Zeng, "Passive Bistatic SAR with GNSS transmitters," in *Bistatic Radar: Emerging Technology*, M. Cherniakov, Ed. New York, NY, USA: Wiley 2008.

[18] M. Antoniou and M. Cherniakov, "GNSS-based SAR: A signal processing view," *EURASIP J. Adv. Sign. Process.*, 2103, 98, pp. 1-16.

[19] F. Santi, M. Antoniou, D. Pastina, "Point Spread Function Analysis for GNSS-based multistatic SAR," *IEEE Geosci. Remote Sens. Lett.*, vol. 12, no. 2, pp. 304-308, Feb. 2015.

[20] F. Santi, M. Bucciarelli, D. Pastina, M. Antoniou, and M. Cherniakov, "Spatial Resolution Improvement in GNSS-Based SAR Using Multistatic Acquisitions and Feature Extraction," *IEEE Transactions on Geoscience and Remote Sensing*, vol. 54, no. 10, pp. 6217-6231, Oct. 2016.

[21] D. Cristallini, M. Caruso, P. Falcone, et al., "Space-based passive radar enabled by the new generation of geostationary broadcast satellites," *IEEE Aerospace Conf.*, 2010, Big Sky, MT, pp. 1-11.

[22] H. Ma, M. Antoniou, M. Cherniakov, "Passive GNSS-Based SAR Resolution Improvement Using Joint Galileo E5 Signals," *IEEE Geoscience and Remote Sensing Letters*, vol. 12, no. 8, pp. 1640 - 1644, Aug. 2015.

[23] M. Antoniou, Z. Hong, Z. Zhangfan, R. Zuo, Q. Zhang, M. Cherniakov, "Passive bistatic synthetic aperture radar imaging with Galileo

transmitters and a moving receiver: experimental demonstration," *IET Radar, Sonar & Navigation*, 2013, vol. 7, no. 9, pp. 985 – 993.

[24] X. He, T. Zeng, M. Cherniakov, "Signal detectability in SS-BSAR with GNSS non-cooperative transmitters," *IET Proc. Radar Sonar Navig.*, vol. 152, no. 3, pp. 124-132, Jun. 2005.

[25] H. Ma, M. Antoniou, M. Cherniakov, et al, "Maritime target detection using GNSS-based passive radar: experimental proof of concept," *2017 IEEE Radar Conference*, Seattle, WA, 2017, pp. 464-469

[26] H. Ma, M. Antoniou, D. Pastina, et al, "Maritime moving target indication using passive GNSS-based bistatic radar," *IEEE Trans. on Aerospace and Electronic Systems*, in press.

[27] F. Pieralice, F. Santi, D. Pastina, et al, "GNSS-based passive radar for maritime surveilance: long integration time MTI technique," *2017 IEEE Radar Conference*, Seattle, WA, 2017, pp. 508-513.

[28] F. Santi, D. Pastina, M. Bucciarelli, "Maritime moving target detection technique for passive bistatic radar with GNSS transmitters," *18th Int. Radar Symp.*, Prague, CZ, 28-30 June 2017.

[29] S. Barbarossa and A. Farina, "Detection and imaging of moving objects with synthetic aperture radar. 2. Joint time-frequency analysis by Wigner-Ville distribution," in *IEE Proceedings F - Radar and Signal Processing*, vol. 139, no. 1, pp. 89-97, Feb 1992.

[30] L. B. Almeida, "The Fractional Fourier Transform and Time-Frequency Representations," in *IEEE Transactions on Signal Processing*, vol. 42, no. 11, pp. 3084-3091, Nov. 1994.

[31] H.-B. Sun, G.-S. Liu, H. Gu, and W.-M. Su, "Application of the Fractional Fourier Transform to Moving Target Detection in Airborne SAR," *IEEE Trans. on Aerospace and Electronic Systems*, vol. 38, no. 4, pp. 1416-1424, Oct. 2002.

[32] A. S. Amein and J. J. Soraghan, "A new chirp scaling algorithm based on the fractional Fourier transform," in *IEEE Signal Processing Letters*, vol. 12, no. 10, pp. 705-708, Oct. 2005.

[33] R. Pelich, N. Longépé, G. Mercier, G. Hajduch and R. Garello, "Vessel Refocusing and Velocity Estimation on SAR Imagery Using the Fractional Fourier Transform," in *IEEE Trans. on Geoscience and Remote Sensing*, vol. 54, no. 3, pp. 1670-1684, March 2016.

[34] C. Clemente; J. J. Soraghan, "Range Doppler and chirp scaling processing of synthetic aperture radar data using the fractional Fourier transform," *IET Signal Processing*, vol. 6, no. 5, pp. 503 - 510, Jul. 2012.

[35] C. Clemente, I. Shorokhov, I. Proudler, et. al, "Radar waveform libraries using fractional Fourier transform," *2014 IEEE Radar Conf.*, Cincinnati, OH, 2014, pp. 855-858.

[36] Z. Li, F. Santi, D. Pastina, and P. Lombardo, "Multi-frame fractional Fourier transform technique for moving target detection with space-based passive radar," *IET Radar Sonar & Navigation*, vol. 11, no. 5, pp. 822-828, May 2017.

[37] J. Frank and J. D. Richard, "Phased Array Radar Antennas," in *Radar Handbook*, 3rd ed., M. Skolnik (Ed.), New York: McGraw-Hill, 2008.

[38] R. P. Perry, R. C. Dipietro, "SAR imaging of moving targets," *IEEE Transactions on Aerospace and Electronic Systems*, vol. 35, no. 1, pp. 188-200, Jan. 1999.

[39] A. Farina, P. Lombardo, L. Ortenzi, "A unified approach to adaptive radar processing with general antenna array configuration," *Signal Processing*, vol. 84, no. 9, 2004, pp. 1593-1623.

Zhongyu Li (S'12) received the B.S. degree in electronic engineering from the University of Electronic Science and Technology of China (UESTC), Chengdu, China, in 2011. He is currently working toward the Ph.D. degree with the School of Electronic Engineering, UESTC.

From November 2015 to November 2016, he was a visiting Ph.D. Student with the Department of Information Engineering, Electronics, and Telecommunications (DIET), University of Roma "La Sapienza," Rome, Italy. His research interests include SAR technology and moving target detection.

Dr. Li serves as the Reviewer of the IEEE TRANSACTIONS ON GEOSCIENCE AND REMOTE SENSING, the IEEE GEOSCIENCE AND REMOTE SENSING LETTERS, and other international technical journals.

Fabrizio Santi received the Master degree (*cum laude*) in telecommunication engineering and the Ph.D. degree in remote sensing from "La Sapienza" University of Rome, Italy, in September 2010 and June 2014, respectively.

From April to September 2013 he carried on research activity with the Microwave Integrated Systems Laboratory, University of Birmingham, U.K. At present, he works as PostDoctoral Researcher at the Department of Information Engineering, Electronics and Telecommunications, "La Sapienza" University of Rome. His main research interests include SAR/ISAR techniques and space-based passive radar systems. The results of his research activity have been reported in a number of journal and conference papers.

Dr. Santi serves as a Reviewer for a number of international technical journals. He received the Best Italian Thesis on Remote Sensing Award from the IEEE Geoscience and Remote Sensing South Italy Chapter in 2010.

Debora Pastina (M'01) received the Laurea degree in telecommunications engineering and the Ph.D. degree in information and telecommunications engineering from "La Sapienza" University of Rome, Rome, Italy, in 1996 and 2000, respectively.

From July 1998 to March 1999, she carried on research activity with the SAR Processing Team, Defence Evaluation Research Agency (DERA), Malvern, U.K. She is currently an Assistant Professor in the DIET Department, "La Sapienza" University of Rome. She is involved and is responsible of scientific research projects funded by the Italian Ministry of Research, by the Italian Space Agency, by the European Commission and by the national radar industry. The results of her activity have been reported in more than 100 journal and conference papers. Her main research interests include SAR/ISAR techniques, GNSS-based passive radar systems, FSR systems and techniques, clutter models, and radar detection in non-Gaussian clutter.

Dr. Pastina was the Chairman of the Local Committee of the IEEE/ISPRS Joint Workshop Urban 2001. She was the Publication Chair of the 2008 IEEE Radar Conference. She is a member of the Editorial Board of the International Journal of Electronics and Communications (AEÜ, Elsevier) and of the IEEE Transactions on Aerospace and Electronic Systems. She has served in the technical review committee of many international conferences and as a Reviewer for a number of international technical journals.

Pierfrancesco Lombardo graduated in1991 at the University of Rome "La Sapienza", Italy. After serving at the Official Test Center of the Italian Air Force, he was associate at Birmingham University (UK) and at Defense Research Agency in Malvern. In 1995 he received his Ph.D and was research associate at Syracuse University (NY-USA). In 1996 he joined the University of Rome "La Sapienza", where he is presently Full Professor.

Dr. Lombardo is involved in, and coordinates, research projects funded by European and National Research Agencies and national industries. He leads the "Radar, Remote Sensing and Navigation" (RRSN) group at the University of Rome "La Sapienza". He chairs the Cosmo SkyMed consulting group for the Italian Space Agency. His main interests are radar adaptive signal processing, radar clutter modelling, radar coherent detection, passive radar and multistatic radar, SAR processing and radio-localization systems. His research has been reported in over 260 publications in international technical journals and conferences.

Dr. Lombardo is associate Editor for Radar Systems for the IEEE Transactions on Aerospace and Electronic Systems (AES) since June 2001 and Technical Editor for Radar System since January 2016. He is member of the IEEE AES Radar System Panel and the Editorial board of IET Proceedings on Radar Sonar and Navigation. He served in the technical committee of many international conferences on radar systems and signal processing. He was Technical Committee Chairman of the IEEE/ISPRS Workshop on Remote Sensing and Data Fusion over Urban Areas URBAN'2001, Rome, URBAN'2003, Berlin, and URBAN'2005, Tempe (US). He was also Technical Chairman of the IEEE Radar Conference 2008. He is co-recipient of the Barry Carlton award (best paper) of IEEE Trans. on AES for year 2001 and of the best paper award for the IEEE Trans. on Geoscience and Remote Sensing for year 2003.